Paleoceanography and Paleoclimatology

AGU ADVANCING EARTH AND SPACE SCIENCE

RESEARCH ARTICLE
10.1029/2022PA004442

Middle Miocene Climate and Stable Oxygen Isotopes in Europe Based on Numerical Modeling

Svetlana Botsyun[1,2], Todd A. Ehlers[1], Alexander Koptev[1,3], Madelaine Böhme[1,4], Katharina Methner[5,6], Camille Risi[7], Christian Stepanek[8], Sebastian G. Mutz[1], Martin Werner[8], Daniel Boateng[1], and Andreas Mulch[5,9]

[1]Department of Geosciences, University of Tübingen, Tübingen, Germany, [2]Institute of Meteorology, Freie Universität Berlin, Berlin, Germany, [3]Helmholtz Centre Potsdam, GFZ German Research Centre for Geosciences, Potsdam, Germany, [4]Senckenberg Centre for Human Evolution and Palaeoenvironment, Tübingen, Germany, [5]Senckenberg Biodiversity and Climate Research Centre, Frankfurt am Main, Germany, [6]Department of Geological Sciences, Stanford University, Stanford, CA, USA, [7]Laboratoire de Météorologie Dynamique, LMD/IPSL, UPMC, CNRS, Paris, France, [8]Alfred Wegener Institute (AWI), Helmholtz Centre for Polar and Marine Research, Bremerhaven, Germany, [9]Institute of Geosciences, Goethe University Frankfurt, Frankfurt am Main, Germany

Key Points:

- A high-resolution isotope-enabled general circulation model is used to explore Middle Miocene climate and precipitation $\delta^{18}O$ across Europe
- Middle Miocene bi-directional precipitation change consistent with herpetological fossils and account for precipitation $\delta^{18}O$ variations
- Global Miocene climate forcing contributed a max $\delta^{18}O$ change of ~2‰ over the high Alpine elevation and to ~1‰ over low elevation

Supporting Information:

Supporting Information may be found in the online version of this article.

Correspondence to:

S. Botsyun,
svetlana.botsyun@fu-berlin.de

Citation:

Botsyun, S., Ehlers, T. A., Koptev, A., Böhme, M., Methner, K., Risi, C., et al. (2022). Middle Miocene climate and stable oxygen isotopes in Europe based on numerical modeling. *Paleoceanography and Paleoclimatology*, *37*, e2022PA004442. https://doi.org/10.1029/2022PA004442

Received 1 MAR 2022
Accepted 3 OCT 2022

Author Contributions:

Conceptualization: Svetlana Botsyun, Alexander Koptev
Data curation: Svetlana Botsyun, Madelaine Böhme
Formal analysis: Svetlana Botsyun
Funding acquisition: Todd A. Ehlers, Sebastian G. Mutz
Investigation: Svetlana Botsyun, Madelaine Böhme, Katharina Methner, Christian Stepanek
Methodology: Svetlana Botsyun, Alexander Koptev, Camille Risi
Software: Martin Werner

Abstract The Middle Miocene (15.99–11.65 Ma) of Europe witnessed major climatic, environmental, and vegetational change, yet we are lacking detailed reconstructions of Middle Miocene temperature and precipitation patterns over Europe. Here, we use a high-resolution (~0.75°) isotope-enabled general circulation model (ECHAM5-wiso) with time-specific boundary conditions to investigate changes in temperature, precipitation, and $\delta^{18}O$ in precipitation ($\delta^{18}O_p$). Experiments were designed with variable elevation configurations of the European Alps and different atmospheric CO_2 levels to examine the influence of Alpine elevation and global climate forcing on regional climate and $\delta^{18}O_p$ patterns. Modeling results are in agreement with available paleobotanical temperature data and with low-resolution Middle Miocene experiments of the Miocene Model Intercomparison Project (MioMIP1). However, simulated precipitation rates are 300–500 mm/yr lower in the Middle Miocene than for pre-industrial times for central Europe. This result is consistent with precipitation estimates from herpetological fossil assemblages, but contradicts precipitation estimates from paleobotanical data. We attribute the Middle Miocene precipitation change in Europe to shifts in large-scale pressure patterns in the North Atlantic and over Europe and associated changes in wind direction and humidity. We suggest that global climate forcing contributed to a maximum $\delta^{18}O_p$ change of ~2‰ over high elevation (Alps) and ~1‰ over low elevation regions. In contrast, we observe a maximum modeled $\delta^{18}O_p$ decrease of 8‰ across the Alpine orogen due to Alpine topography. However, the elevation-$\delta^{18}O_p$ lapse rate shallows in the Middle Miocene, leading to a possible underestimation of paleotopography when using present-day $\delta^{18}O_p$—elevation relationships data for stable isotope paleoaltimetry studies.

1. Introduction

The Middle Miocene (15.99–11.65 Ma) was a time of major climatic, tectonic, environmental, and vegetation change (Herold et al., 2008; Steinthorsdottir et al., 2021). Proxy records, including global compilations of benthic $\delta^{18}O$ and $\delta^{13}C$ values (e.g., Foster & Rohling, 2013; Wright et al., 1992), indicate a shift from a period of relatively warm global conditions during the Miocene Climatic Optimum (MCO) (16.75–14.5 Ma) to the less warm Middle Miocene Climate Transition (MMCT) starting at ~14.7 Ma. Paleoclimate proxy records document sub-modern to moderately high atmospheric pCO_2 values (~180–600 ppm) during the Middle Miocene (Foster & Rohling, 2013; Pagani et al., 1999), with possibly elevated pCO_2 levels of 350–630 ppm (Cui et al., 2020; Greenop et al., 2014; Sosdian et al., 2018; Steinthorsdottir et al., 2021) or up to ~600 ppm with over 1,000 ppm permissible (Rae et al., 2021) during the MCO. In addition, during the MCO, sea surface temperatures (SSTs) were 8°C–10°C warmer than today in the high southern latitudes (Shevenell et al., 2008) and 10°C–15°C warmer in the high northern latitudes (Super et al., 2018, 2020). In contrast, the MMCT was a period when SSTs were similar to present-day (Steinthorsdottir et al., 2021). Middle Miocene glaciation was unipolar, with a substantial reduction in Antarctic ice volume during the MCO (Feakins et al., 2012; Westerhold et al., 2005) and a large expansion of the Antarctic ice sheet volume, comparable to the present-day, during the MMCT (Langebroek et al., 2009, 2010). The aforementioned climate changes during the Middle Miocene had diverse implications for terrestrial settings globally, including Europe, which is the focus of this study.

Supervision: Todd A. Ehlers, Andreas Mulch
Validation: Madelaine Böhme, Katharina Methner, Christian Stepanek, Martin Werner, Andreas Mulch
Visualization: Svetlana Botsyun, Todd A. Ehlers, Alexander Koptev, Daniel Boateng
Writing – original draft: Svetlana Botsyun
Writing – review & editing: Todd A. Ehlers, Alexander Koptev, Madelaine Böhme, Katharina Methner, Camille Risi, Christian Stepanek, Sebastian G. Mutz, Martin Werner, Daniel Boateng, Andreas Mulch

Although global climate change during the Miocene is relatively well documented for the marine realm (Gaskell et al., 2022), limited information is available concerning terrestrial climate change (Steinthorsdottir et al., 2021). Moreover, the Miocene has been proposed as a potential analog for future climate scenarios (Steinthorsdottir et al., 2021), making Miocene climate reconstructions from both proxies and models strategically important. However, the mechanisms behind climate change around the Middle Miocene are poorly understood for Europe and warrant further investigation. Although the Miocene climate of Europe has been extensively investigated (e.g., Bruch et al., 2007 and references herein; Bouchal et al., 2018; Methner et al., 2020; Worobiec et al., 2021), paleoclimate data are in parts still controversial. For example, estimates of Middle Miocene precipitation from herpetological fossil assemblages (Böhme et al., 2011) suggest lower precipitation amounts around 300–500 mm/yr less than today. However, these estimates are at odds with plant proxy data showing wetter conditions than today in Central and Eastern Europe with precipitation rates up to 1,400 mm/yr (Bruch et al., 2011). Despite recent advances in simulating Miocene climate (Burls et al., 2021), models have difficulty reproducing the magnitude of warming (Burls et al., 2021), and high-resolution regional studies that better capture orographic effects (Acosta & Huber, 2017, 2020) are still lacking. Moreover, little is known about the dynamics of the hydrological cycle and atmospheric circulation (Eronen et al., 2012; Methner et al., 2020; Quan et al., 2014). Therefore, new high-resolution modeling studies are essential to reconcile different proxy data with each other and with modeling results.

The Miocene was a period of continued mountain building and surface uplift for the European Alps (e.g., Eizenhöfer et al., 2021; Handy et al., 2010; Schmid et al., 1996; Valla et al., 2021). Surface uplift of the Alps has previously been suggested to influence European climate (Botsyun et al., 2020; Campani et al., 2012; Krsnik et al., 2021; Boateng et al., 2022), but detailed time-specific studies quantifying the magnitude of spatial and temporal variations and dynamics of regional climate change are still lacking. Moreover, the timing and rate of the surface uplift of the Alps is still controversial and ranges from reconstructed elevations of 1,900 ± 1,000 m (Schlunegger & Kissling, 2015) to elevations >4,000 m (Jäger & Hantke, 1984; Krsnik et al., 2021; Sharp, 2005). Thus, in order to reconstruct past climate in Europe, the elevation history of the Alps plays a key role.

Among the methods developed to determine the uplift history of orogens, stable isotope paleoaltimetry is the most commonly used. This method is based on a systematic relationship between the oxygen or hydrogen isotopic ratios of precipitation ($\delta^{18}O_p$, δD_p) and elevation (Poage & Chamberlain, 2001; Rowley et al., 2001). However, both global and regional climate change as a consequence of mountain uplift may contribute to $\delta^{18}O_p$ patterns used in paleoelevation reconstructions (Botsyun & Ehlers, 2021; Botsyun et al., 2016, 2019; Ehlers & Poulsen, 2009; Insel et al., 2012; Mulch, 2016; Poulsen et al., 2010). The sensitivity of $\delta^{18}O_p$ to regional, global, and topographic variations in paleotemperature, environmental conditions of an air mass prior to orographic ascent, evapotranspiration, vegetation changes, water vapor recycling, and changes in vapor source have been shown to contribute to the uncertainty of elevation reconstructions (Botsyun & Ehlers, 2021; Botsyun et al., 2020; Kukla et al., 2019; Mulch, 2016). Therefore, a rigorous reconstruction of the elevation history of the Alps requires careful consideration of both regional and global climate drivers.

Modeling strategies using high-resolution isotope-enabled general circulation model (GCMs) together with time-specific boundary conditions have become a powerful tool not only for reconstructing global and regional paleoclimates but also for enhancing elevation reconstructions from $\delta^{18}O_p$ proxy data (Botsyun & Ehlers, 2021). In this study, we complement previous work by providing high-resolution (T159, ∼0.75° per grid cell) isotope-enabled GCM experiments with Middle Miocene boundary conditions and investigate temperature, precipitation, and the $\delta^{18}O_p$ pattern over the European continent. We compare model predictions with independent sources of information—first, with the result from models within the Miocene Model Intercomparison Project (MioMIP1), and second, with climate characteristics derived from proxy data. In our experiments, we investigate not only the effects of long-term global cooling during the MMCT, including a drop of atmospheric CO_2 concentration and the impact of an expanded Antarctic ice sheet on climate in Europe, but also the contribution of local geographic changes, such as the uplift of the Alps and the retreat of the Paratethys Sea. We test the hypothesis that global and regional forcing resulted in temperature, precipitation, and humidity changes that in turn affect $\delta^{18}O_p$ changes across Europe. We pursue two goals that are closely related, since there is a close relationship between mountain elevations, climate, and $\delta^{18}O_p$. We aim to: (a) investigate Middle Miocene climate in Europe under global and regional forcing and to explain the inconsistencies between different terrestrial proxy records in Europe, and (b) demonstrate the link between regional $\delta^{18}O_p$ patterns and paleoclimatic changes in Europe and show consequences for paleoelevation estimates of the Alps. We discuss (a) the large-scale drivers of

climate change in Europe, (b) the sources of discord between GCM predictions of European climate change and different terrestrial proxy records, (c) the implications of global climate change and Alpine surface uplift on the $\delta^{18}O$ records and paleoclimate proxy records in Europe, and (d) the consequences of changes in paleoclimate and $\delta^{18}O_p$ for paleoelevation estimates of the Alps.

2. Background

Tectonic uplift of mountain belts (Raymo & Ruddiman, 1992; Ruddiman & Kutzbach, 1989), as well as smaller orogens, such as the European Alps (Botsyun et al., 2020; Boateng et al., 2022) have been shown to be important for global and regional climate. The Late Cretaceous to Paleogene closure of the Alpine Tethys, the collision between the Adriatic and the European continental plates (Handy et al., 2010; Schmid et al., 1996; Stampfli et al., 1998) and subsequent post-collisional convergence (e.g., Schmid et al., 1996) ultimately resulted in the surface uplift of the Alps. However, the timing and rate of this uplift is still controversial, with Miocene stable-isotope-based paleoelevation estimates ranging from mean elevations of 1,900 ± 1,000 m (Schlunegger & Kissling, 2015) and 2,300 ± 650 m (Kocsis et al., 2007) to 2,850 + 800/-600 m (Campani et al., 2012), and >4,000 m (Krsnik et al., 2021; Sharp, 2005). Based on combined evidence from sediment budget curves, thermochronology, and sediment facies, the maximum elevation of the Western and central Alps has been estimated at 2,500–3,000 m for the middle Miocene (Kuhlemann, 2007). Very high Alps (>5,000 m) already at the Oligocene-Miocene boundary were inferred by Jäger and Hantke (1984) based on large erratic boulders found at great distances from their place of origin. These estimates, however, contradict geomorphologic and sediment budget-based modeling studies suggesting that present-day elevations of the Alps were attained only at ∼5–6 Ma while Miocene topography was still much lower (Hergarten et al., 2010). Depending on its topographic structure, the impact of the Alpine orogen on regional climate would be different, thus quantitative estimates of the surface elevation of the Alps are extremely important.

Modern efforts to model Miocene climate have recently been combined into a multi-model ensemble of MioMIP1 and are critically reviewed in Burls et al. (2021) and summarized in Steinthorsdottir et al. (2021). Elements other than CO_2, such as Miocene paleogeography and ice sheets, have been shown to contribute to the global mean temperature increase of ∼2°C (Burls et al., 2021) compared to pre-industrial times. In general, previous models with realistic CO_2 concentrations have had difficulty to reproduce the magnitude of warming indicated by proxy data. The models used in MioMIP1 represent the state-of-the-art in modeling of the Miocene epoch, however, they are inhomogeneous (in terms of both experimental design and model physics/parameterization) and not ideal for formal inter-model comparison, as Burls et al. (2021) acknowledge. Furthermore, these model simulations were performed at low spatial resolution (T31 or T42, corresponding to a grid spacing of ∼3.75° or ∼2.79°, respectively), since high-resolution paleoclimate simulations are timely and computationally expensive, and do not focus specifically on interpreting climate variations across Europe.

3. Methods

3.1. Model and Experimental Design

We apply the isotope-enabled version (ECHAM5-wiso; Werner et al., 2011) of the atmospheric GCM ECHAM5 developed at Max Planck Institute for Meteorology (Roeckner et al., 2003). The ECHAM5 model incorporates the Subgrid Scale Orographic Parameterization developed by Lott (1999) and Lott and Miller (1997). This parameterization represents the effects of orographic variations at scales smaller than the horizontal resolution of the grid (Roeckner et al., 2003). As an integral part of the climate simulation, the water isotopes (HDO, $H_2^{16}O$, and $H_2^{18}O$) in ECHAM5-wiso undergo kinetic and equilibrium fractionation during phase transitions (e.g., vapor, cloud, snow, etc.) in the atmosphere (Werner et al., 2011). The climate component of ECHAM5-wiso, employed without isotopes, has been shown to capture the large-scale features of global climate reasonably well (e.g., Knorr et al., 2011; Mutz et al., 2018). For the present-day climate, high-resolution ECHAM5-wiso experiments successfully reproduce observed precipitation, temperature, and $\delta^{18}O_p$ patterns on both annual and seasonal scales in Europe (Botsyun et al., 2020; Langebroek et al., 2011). However, the model tends to underestimate the present-day precipitation over the Alpine region, especially in summer. ECHAM5-wiso has also been successfully used for paleoclimate simulations (Pliocene and Last Glacial Maximum) and validated for the European region (Botsyun et al., 2020).

We used three ECHAM5-wiso topography sensitivity experiments with pre-industrial boundary conditions described in detail in Botsyun et al. (2020) and performed nine new ECHAM5-wiso experiments with Middle Miocene boundary conditions. The summary of the experiments is shown in Table 1. The control simulation (pre-industrial, PI) is the same as in Botsyun et al. (2020) and Mutz et al. (2018) (their Alps100 experiment) and used pre-industrial boundary conditions (e.g., insolation, greenhouse gases, SSTs) and present-day Alpine topography. This experiment was forced by monthly mean climatology of SSTs and sea ice concentrations (SICs), derived from a low-resolution transient coupled ocean-atmosphere simulation (Lorenz & Lohmann, 2004) conducted for the same time period with a pCO_2 level set to 280 ppm. Land surface parameters for the PI simulation, including vegetation are based on Hagemann (2002).

Three steps underlie our analysis. First, we used the sensitivity experiments of topographic changes of the European Alps from Botsyun et al. (2020). All boundary conditions, including albedo, surface roughness length, and vegetation distribution, are identical to those in the PI simulation, but in one simulation elevation is reduced to 250 m in the area covering the Alps and Alpine foreland (PI_noAlps; equivalent to Alps0 in Botsyun et al., 2020) and in one simulation increased to 150% of the present elevations in the same region (PI_plusAlps; equivalent to Alps150 in Botsyun et al., 2020). The PI_plusAlps experiment was conducted to test the sensitivity of the climate in Europe to significantly higher-than-present Alpine elevations, as suggested by Krsnik et al. (2021).

Second, we conducted two experiments with Middle Miocene boundary conditions reflecting two pCO_2 settings (278 and 450 ppm; Mio_278 and Mio_450 experiments) within current estimates of the Middle Miocene pCO_2 (Foster & Rohling, 2013; Sosdian et al., 2018; Steinthorsdottir et al., 2021). These two pCO_2 settings approximately reflect MCO and MMCT climatic states, with Mio_450 ppm representing the MCO and Mio_278 representing the MMCT. We highlight that we chose the Mio_450 experiment conservatively to rather underestimate pCO_2 conditions during the MCO. In addition to greenhouse gas concentrations (pCO_2, pCH_4, pN_2O), the paleoclimate simulations account for changing terrestrial ice sheets, vegetation cover, albedo, orbital variations, SSTs, and SICs (Table 1). We use the SSTs and SICs, generated by the low-resolution fully coupled atmosphere-ocean COSMOS model experiments with Middle Miocene boundary conditions (Huang et al., 2017; Stärz et al., 2017; their Mio_278 and Mio_450 experiments). Corresponding COSMOS experiments were part of the MioMIP1 comparison (Burls et al., 2021). Physical soil properties, such as soil albedo and maximum water holding field capacity are derived by adapting vegetation-related parameters computed by a dynamic vegetation module (Brovkin et al., 2009) of the global land surface and carbon cycle model JSBACH (Raddatz et al., 2007) as part the fully coupled atmosphere-ocean model COSMOS. Orography-related variables were derived from the paleogeographic reconstruction of Herold et al. (2008). Although geography of the Middle Miocene and present are remarkably similar, the Middle Miocene reconstruction has several notable modifications, including rotation of continents, altered ocean gateways, and height of major orogens (Figure 1a). For ECHAM5-wiso simulations, the $\delta^{18}O$ values of ocean surface waters have to be prescribed as a model boundary condition. The lack of seawater $\delta^{18}O$ from COSMOS coupled simulations and sparse observational data have prevented us from the construction and use of a comprehensive global gridded data set of $\delta^{18}O$ for the Middle Miocene. For the Mio_450 and Mio_278 simulations, the seawater $\delta^{18}O$ values were set identically to present-day. In order to test the sensitivity of Middle Miocene $\delta^{18}O_p$ in Europe to changes of ocean surface waters $\delta^{18}O$, we performed two additional simulations (Mio_278_iniwiso, Mio_450_iniwiso) in which, the $\delta^{18}O$ values of ocean surface waters have been computed from the salinity of the upper ocean level of corresponding COSMOS coupled simulations using the relationships from Paul et al. (1999) (Figure S1 in Supporting Information S1). Close agreement between model-simulated $\delta^{18}O$ of ocean surface water and $\delta^{18}O$ values derived from water salinity is shown by Gaskell et al. (2022) (their Sup Figure 7).

Third, for both Middle Miocene pCO_2 settings, we conduct three sensitivity experiments to investigate the effects of Alpine topography and marine transgression/regression in Europe (Table 1, Figure 1). We study the effects of surface uplift of the Alps by increasing and decreasing their elevation, similar to the pre-industrial sensitivity experiments. We reduce the elevation in the area covering the Alps and the Alpine forelands to 250 m elevation (Mio_278_noAlps, Mio_450_noAlps; Figure 1d) and increase the elevation to twice the reconstructed height (Mio_278_plusAlps, Mio_450_plusAlps; Figure 1e) compared to the original paleogeographic reconstruction of Herold et al. (2011) (used in Mio_278 and Mio_450 experiments), which reflects recent hypotheses of very high Alpine elevations in the Middle Miocene (Krsnik et al., 2021). We also tested the influence of a marine transgression and regression within Europe on regional climate and stable water isotopes. For this purpose, we performed two additional experiments (Mio_278_SeaLand and Mio_450_SeaLand) with modified land-sea distributions

Table 1
ECHAM5-wiso Experiments Summary

Experiment name	Greenhouse gases concentration	Orbital parameters	Surface conditions	Alps elevation
PI	CO_2 280 ppm, CH_4 760 ppb, N_2O 270 ppb.	Eccentricity = 0.016804, obliquity = 23.4725, longitude of perihelion = 278.734	Sea surface temperature and sea ice are taken from a transient low-resolution coupled ocean-atmosphere simulation (Dietrich et al., 2013; Lorenz & Lohmann, 2004). Land surface parameters, including vegetation are based on (Hagemann, 2002).	100% of present
PI_noAlps	Same as PI	Same as PI	Same as PI	Reduced to 250 m
PI_plusAlps	Same as PI	Same as PI	Same as PI	Increased by 50%
Mio_278	CO_2 278 ppm, CH_4 650 ppb, N_2O 270 ppb.	Eccentricity = 0.016724, obliquity = 23.4468, longitude of perihelion = 272.157	Sea surface temperature, sea ice and vegetation from Middle Miocene COSMOS (278 ppm) simulations (Stärz et al., 2017). Paleogeography from Middle Miocene reconstruction (Herold et al., 2011). The height of the Antarctic ice-sheet is reduced compared to present-day (Herold et al., 2008) and the Greenland ice-sheet is absent. Seawater $\delta^{18}O$ values were set identical to present-day. Physical soil characteristics, such as soil albedo and maximum water holding field capacity, derived by adapting vegetation related parameters based on (Stärz et al., 2017).	100% of present
Mio_278_noAlps	Same as Mio_278	Same as Mio_278	Same as Mio_278	Reduced to 250 m
Mio_278_plusAlps	Same as Mio_278	Same as Mio_278	Same as Mio_278	Increased by 100%
Mio_278_iniwiso	Same as Mio_278	Same as Mio_278	Same as Mio_278, except for seawater $\delta^{18}O$ values, which were computed from upper-level ocean salinity from COSMOS (278 ppm) simulations (Stärz et al., 2017) using the relationships from (Paul et al., 1999).	100% of present
Mio_278_LanSea	Same as Mio_278	Same as Mio_278	Same as Mio_278, except for the Paratethys Sea area, which extends in accordance to Popov et al. (2004).	100% of present
Mio_450	CO_2 450 ppm, CH_4 650 ppb, N_2O 270 ppb.	Eccentricity = 0.016724, obliquity = 23.4468, longitude of perihelion = 272.157	Sea surface temperature, sea ice and vegetation from Middle Miocene COSMOS (450 ppm) simulations (Stärz et al., 2017). Paleogeography from Middle Miocene reconstruction (Herold et al., 2011). The height of the Antarctic ice-sheet is reduced compared to present-day (Herold et al., 2008) and the Greenland ice-sheet is absent. Seawater $\delta^{18}O$ values were set identical to present-day. Physical soil characteristics, such as soil albedo and maximum water holding field capacity, derived by adapting vegetation related parameters based on (Stärz et al., 2017).	100% of present
Mio_450_noAlps	Same as Mio_450	Same as Mio_450	Same as Mio_450	Reduced to 250 m
Mio_450_plusAlps	Same as Mio_450	Same as Mio_450	Same as Mio_450	Increased by 100%
Mio_450_iniwiso	Same as Mio_450	Same as Mio_450	Same as Mio_450, except for seawater $\delta^{18}O$ values, which were computed from upper-level ocean salinity from COSMOS (450 ppm) simulations (Stärz et al., 2017) using the relationships from (Paul et al., 1999).	100% of present
Mio_450_LandSea	Same as Mio_450	Same as Mio_450	Same as Mio_450, except for the Paratethys Sea area, which extends in accordance to Popov et al. (2004).	100% of present

Note. PI, pre-industrial.

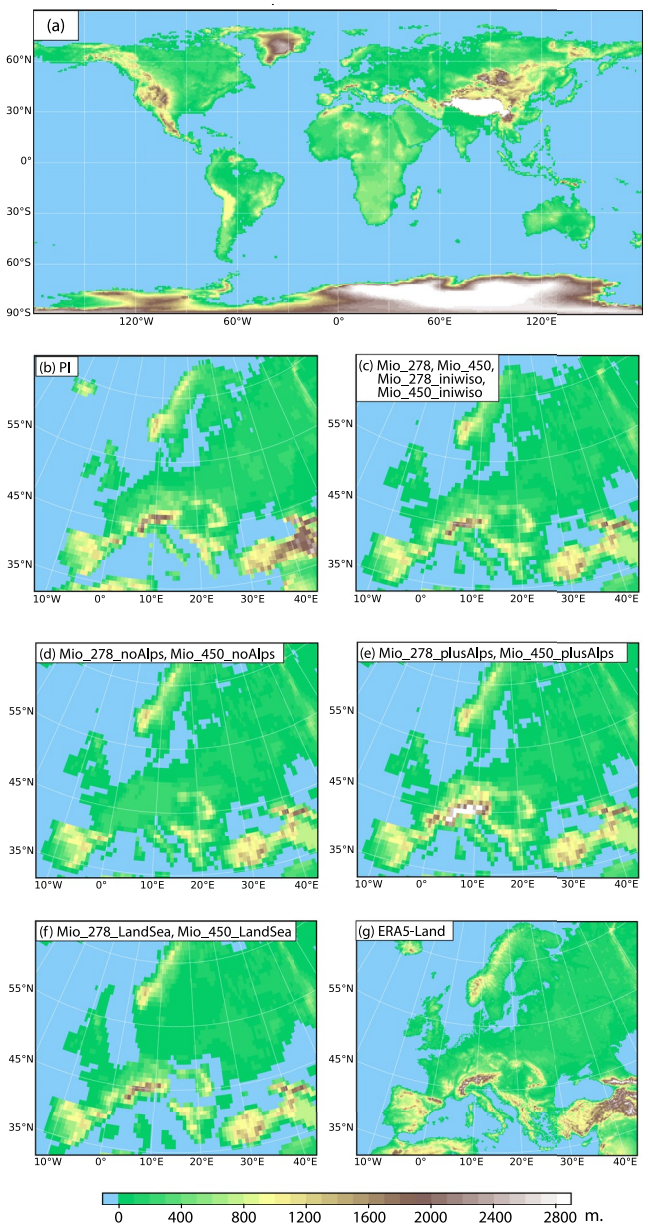

Figure 1. (a) Global Middle Miocene paleogeography of Herold et al. (2008) at T159 model resolution, used in the following experiments: Mio_278, Mio_450, Mio_278_iniwiso, and Mio_450_iniwiso experiments; (b) present-day topography of Europe at T159 model resolution, (c) same as subplot (a) but for the European region; (d) modified Middle Miocene paleogeography with Alpine elevation reduced to 250 m compared to the original reconstruction of Herold et al. (2008), applied in Mio_278_noAlps and Mio_450_noAlps experiments; (e) modified Middle Miocene paleogeography with increased Alpine elevation by 100% compared to the original reconstruction of Herold et al. (2008), applied in the Mio_278_plusAlps and Mio_450_plusAlps experiments; (f) modified Middle Miocene paleogeography, with the land-sea distribution in the European region according to Popov et al. (2004), applied in Mio_278_LandSea and Mio_450_LandSea experiments; (g) topography from ERA5-Land data set (Muñoz-Sabater et al., 2021).

over Europe (Figure 1f), corresponding to the mid-Middle Miocene reconstruction (14 Ma) from the Paleogeographic Atlas of the Paratethys region (Popov et al., 2004).

All experiments were performed at high resolution (T159 L31, corresponding to a grid spacing of ∼0.75°, or ∼80 km in latitude and longitude at the equator, with 31 vertical levels up to 10 hPa). A further increase in model resolution, which would be required for a better representation of the topography, was not possible due to limited computing resources. Each model experiment was run for 13 model years. For lower resolutions of the model, simulation in an atmosphere-only setup forced with SST and SIC, has been shown to quickly bring the model into quasi-equilibrium, not instantaneously, but within the first two to three model years (Stepanek & Lohmann, 2012). Therefore, we consider the results of the experiments from the fourth model year onwards. In the Mio_278 and Mio_450 experiments, the climate appears to deviate slightly from radiative equilibrium, with an average net energy imbalance of ∼−4.2 W/m^2 and ∼−6.7 W/m^2. Since the atmosphere cannot generate energy, the SSTs, provided to the model from a quasi-equilibrium simulation of the model that has been coupled at lower resolution to an ocean model, are too warm for the high-resolution atmosphere standalone model in combination with the prescribed radiative forcing. This is a common problem in atmosphere standalone simulations (e.g., Stepanek & Lohmann, 2012). The year-to-year fluctuations of temperatures for both Mio_278 and Mio_450 are of the same order of magnitude as in the modern observations (by up to 0.1°C–0.2°C per year), and the trends (decreasing for Mio_278 and increasing for Mio_450) are small (∼0.01°C/yr), therefore, we consider our model experiment to be sufficiently equilibrated. We analyzed computed climatological values and inter-annual variations of the last 10 model years for each experiment.

3.2. Post-Processing

Our analyses are based on daily and seasonal averages of temperature, precipitation, evaporation, humidity, sea level pressure (SLP), winds, vertical velocity (ω) at 500 hPa level, δ^{18}O in vapor ($\delta^{18}O_v$), and $\delta^{18}O_p$ values. These outputs are presented after calculating arithmetic means of the 6-hourly ECHAM5-wiso output. In the analysis of vertical motion of air, high subsidence areas were detected by positive ω as well as low relative humidity. We provide a detailed analysis for three regions in Europe (Figure 2a, black rectangles): (a) central Europe including the Alpine region (from 40°N to 55°N and from 2°W to 25°E), (b) a low-elevation region (from 48°N to 51°N and from 2°E to 16°E; all grid cells lower than 500 m), and (c) a high-elevation region (from 42°N to 48°N and from 2°E to 16°E; all grid cells higher than 1,000 m).

3.3. Proxy Data Compilation of Terrestrial Temperature and Precipitation

GCM model predictions are compared to a literature compilation of Middle Miocene terrestrial proxy data for paleotemperature and paleoprecipitation from Europe provided by various previous publications (Tables S1 and S2). We use the compilation of European mean annual temperature (MAT) proxy data from Burls et al. (2021) for the Middle Miocene (Table S1). These values were supplemented with estimates of the mean temperature of the warmest month (WMT) and mean temperature of the coldest month (CMT)

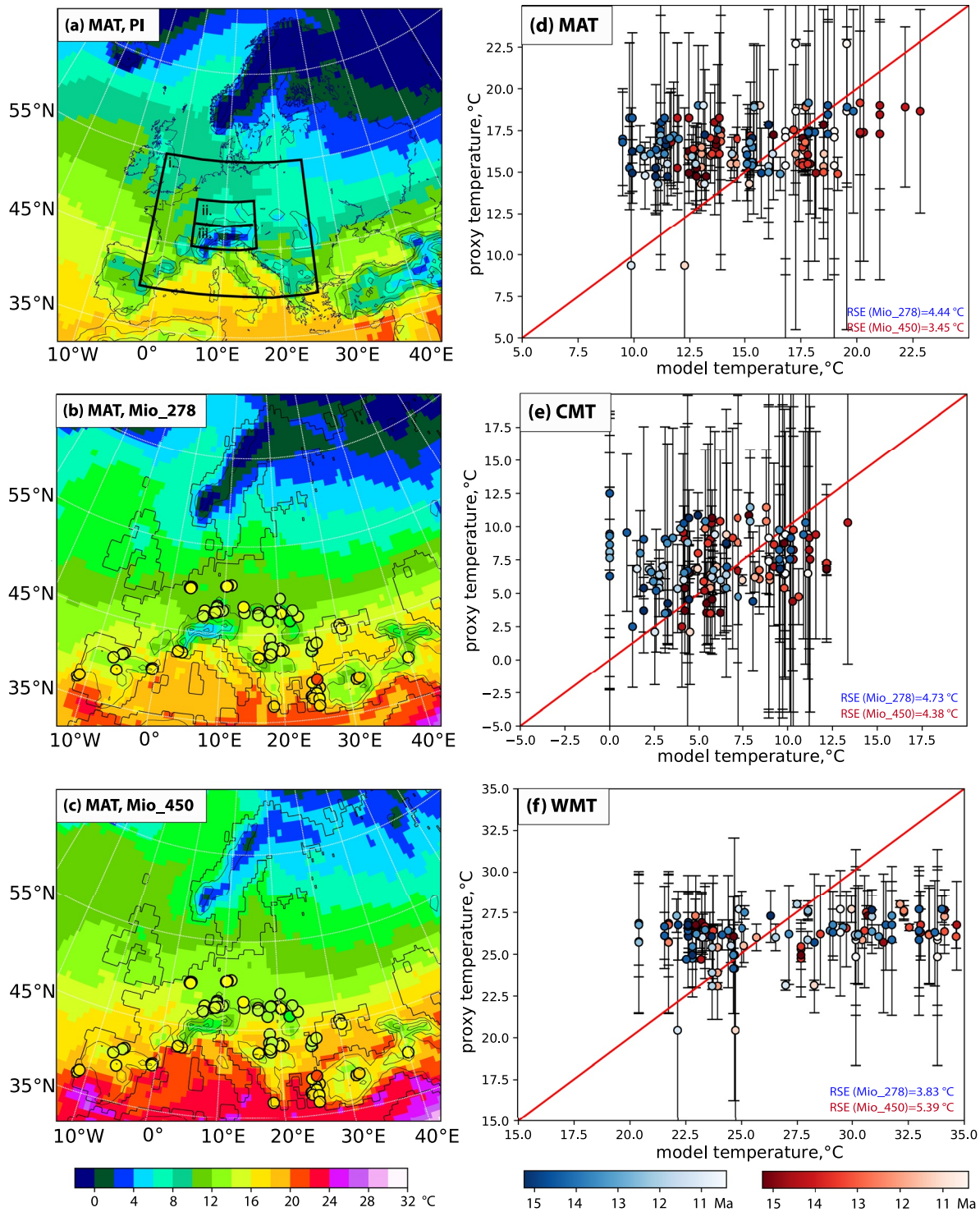

Figure 2.

when available from the original publications. Paleotemperature estimates (Table S1) presented here come from fossil plant data and are based on the coexistence approach. This method uses the modern climatic range of a fossil taxon's nearest living relative to determine the climatic parameters of its habitat and in a second step determines the climatic envelope of coexisting species of an entire fossil assemblage (Mosbrugger & Utescher, 1997; Utescher et al., 2014).

The compilation of mean annual precipitation (MAP) is presented separately in two tables (Tables S1 and S2) depending on the estimation approach. Table S1 contains MAP values reconstructed from fossil plant data using the coexistence approach. This table additionally contains estimates of monthly mean precipitation of the driest month (highest monthly precipitation, LMP) and monthly mean precipitation of the wettest month (lowest monthly precipitation, HMP) when available from the original publications. Table S2 contains the herpetological assemblages presented in Böhme et al. (2007, 2011), with addition of new sites from Böhme and Vasilyan (2014). For both the paleotemperature and the paleoprecipitation databases, all site coordinates were rotated to their position in the middle Miocene using the GPLATES online tool (http://portal.gplates.org/service/) based on individually averaged age estimates for each data point.

3.4. Comparison to Reanalysis and to Previous Models

To evaluate our ECHAM5-wiso PI experiment, we compare our results with the ERA-Interim reanalysis (Dee et al., 2011) for the European region. With this comparison, we aim to show (a) the similarity of the present-day and PI spatial patterns across Europe at the annual-mean and seasonal scale, and (b) the changes between PI and modern conditions. To evaluate our simulations of the Middle Miocene, we compare our simulated temperature and temperature difference between the Middle Miocene and the PI experiments with the simulated values reported in Burls et al. (2021) for MioMIP1. We caution readers that this is not a formal model intercomparison, because the experiments presented in Burls et al. (2021) and our experiments are inhomogeneous. Apart from the obvious differences in CO_2 forcing, the differences lie in (a) the length of the analysis periods, ranging from 10 years (ECHAM5-wiso) to >100 years in Burls et al. (2021), (b) the model complexity, from atmosphere-only (ECHAM5-wiso) to fully coupled (e.g., CCSM3, HadCM3L, COSMOS, IPSLCM), and (c) the model resolution, from low-resolution (T31 or T42) experiments in Burls et al. (2021) to high-resolution (T159) ECHAM5-wiso experiments.

3.5. Comparison of Model Predictions and Proxy Data

We provide a simple statistical analysis in order to compare proxy data and model outputs. With this aim, we adjust the parameters of a model function ($y = f(x)$) to a data set, where x is MAT, WMT, CMT, MAP, LMP, and or HMP, respectively, from our proxy data compilation, and y is MAT, WMT, CMT, MAP, LMP, or HMP, respectively, simulated by ECHAM5-wiso. Then, for each pair of x and y, the residual standard error (RSE) is calculated, which permits us to identify the optimal model-data fit, which occurs when the RSE is minimized.

4. Results

4.1. Comparison of Simulated Temperature With Models Participating in MioMIP1

We compare our simulated Middle Miocene temperature (Figure 2) and the temperature difference between Middle Miocene and PI runs with the simulated values reported in Burls et al. (2021). From this publication, we choose the experiments with CO_2 concentrations in the range of 200–280 and 400–450 ppm to compare with our Mio_278 and Mio_450 experiments, respectively. For brevity in the main text, we include the comparison of our simulations with the MioMIP1 simulations in the supplementary material (Figures S2 and S3 in Supporting Information S1).

Figure 2. Maps of mean annual temperature (MAT) for (a) PI, (b) Mio_278 and (c) Mio_450 experiments. Shaded circles on (b and c) show Middle Miocene MAT (as the mean between MAT max and MAT min), compiled from terrestrial paleobotany proxy data (see Table S1). Isolines show topography for experiments PI, Mio_278 and Mio_450; isolines are with a 500 m contour interval. Black rectangles on subplot (a) show selected regions: (i) central Europe and Alpine region (from 40°N to 55°N and from 2°W to 25°E; grid cells over the continent only), (ii) low-elevation region (from 48°N to 51°N and from 2°E to 16°E; all grid cells lower than 500 m), (iii) high-elevation region (from 42°N to 48°N and from 2°E to 16°E; all grid cells higher than 1,000 m). Subplot (d) model mean annual temperature (MAT), (e) model coldest month temperature (CMT) and (f) model warmest month temperature (WMT) model vs. corresponding values reconstructed using the coexistence approach on paleofloral data. For the comparison with the two Miocene simulations (Mio_278 and Mio_450), the corresponding data (without subdivision by age) are taken from Table S1. Model values in subplots (d–f) are taken at sample locations. The bluish colors show all points data when compared to the Mio_278 temperatures and the reddish colors when compared to the Mio_450 temperatures. Color intensity corresponds to the averaged absolute age of the data point (see Table S1): light blue and light red—younger age, dark blue and dark red—older age. The red line shows a 1:1 model-data fit. RSE, residual standard error between proxy data and model temperature. Points restored to their paleo coordinates by means of GPLATES online tool (http://portal.gplates.org/service/).

Results indicate that ECHAM5-wiso reproduces global MATs compared to the Middle Miocene model experiments involved in MioMIP1 (Burls et al., 2021; Figures S2 and S3 in Supporting Information S1; Table S3 in Supporting Information S1). For the Mio_278 simulation, the global mean annual surface temperature is 2.5°C higher than for PI (Table S3 in Supporting Information S1). This is higher than values reported in Burls et al. (2021) for experiments with CO_2 concentration of 200–280 ppm, which provide the multi-model mean of 1.5°C (Table S3 in Supporting Information S1). For the Mio_450 experiment, the global mean annual surface temperature is 5.9°C higher than for PI (Table S3 in Supporting Information S1). This lies in the high-end of values presented in Burls et al. (2021) for experiments with CO_2 concentration of 400–450 ppm (Table S3 in Supporting Information S1). We note that our modeled temperature anomaly is within the uncertainty range of the MioMIP1 simulations. Particularly pronounced (positive) anomalies are found with respect to simulations based on the HadCM3L model. This model has been shown, however, to produce comparatively cold simulations within the MioMIP1 ensemble (Figure 4a by Burls et al., 2021).

At a regional scale, over central Europe and the Alpine region, (region (i) in Figure 2a), the mean temperature difference between Mio_278 and the multi-model mean temperature from MioMIP1 experiments at 200–280 ppm is 2.7°C (Table S3 in Supporting Information S1). The regional mean temperature difference between Mio_450 and the multi-model mean temperature from MioMIP1 experiments at 400–450 ppm is 1.9°C. For both CO_2 setups, ECHAM5-wiso systematically shows higher temperatures (up to max. 4°C) over the low-elevation region (region (ii) in Figure 2a). Lower temperatures (up to max. 10°C) are simulated over the high-elevation region (region (iii) in Figure 2a), and also over Carpathians, Dinarids and other mountainous regions in Europe (Figures S2 and S3 in Supporting Information S1).

4.2. ECHAM5-Wiso Simulated Middle Miocene MAT

We first discuss the simulated near-surface MAT in the Middle Miocene control experiments (Mio_278 and Mio_450) and compare those with European plant fossil-derived MAT (based on coexistence approach, see Section 3.3). Finally, we examine changes in simulated near-surface MAT of the Middle Miocene experiments that result from varied elevation of the European Alps.

The simulated MAT over the central Europe and the Alpine region (Figure 2a, region (i)) is 12.0°C and 15.0°C in the Mio_278 and Mio_450 experiments, respectively (Figures 2a–2c; Table S4 in Supporting Information S1). The largest difference relative to PI is over the high-elevation region (elevations >1,000 m), which is 3.4°C and 7.2°C warmer in the Mio_278 and Mio_450 experiments, respectively. The Mio_450 simulation shows good agreement with MAT reconstructed by the coexistence approach on fossil plants, while the Mio_278 simulation shows generally lower temperatures than predicted by the coexistence approach (Figure 2d, Table S4 in Supporting Information S1). The model-proxy data fit estimated using the RSE method is 4.4°C for the Mio_278 and 3.5°C for Mio_450 (Table S5 in Supporting Information S1). Thus, the simulation with higher pCO_2 concentration shows a better fit to fossil plant data.

Experiments with varied elevation of the Alps show that most temperature changes are restricted to the Alpine region itself (Figures 3a–3d). Experiments with higher Alpine elevations (Mio_278_plusAlps, Mio_450_plusAlps) show 4.1°C and 3.3°C lower temperatures over high-elevation region of the Alps, compared to Mio_278 and Mio_450, respectively (Table S4 in Supporting Information S1). In contrast, over the low-elevation regions, this decrease is minimal with 0.9°C and 0.1°C, respectively. The temperature increase in the experiments with reduced Alpine elevation (Mio_278_noAlps, Mio_450_noAlps) compared to Mio_278 and Mio_450 is less than 1°C for the central Europe region and the low-elevation region, but is up to 4.4°C (Mio_278) and 4.3°C (Mio_450) for the high-elevation region. The temperature change over both the low-elevation and the high-elevation region in the Mio_278_LandSea and Mio_450_LandSea simulations compared to the Miocene control simulation (Mio_278 and Mio_450, respectively) is less than 1°C (Figure 3e; Table S4 in Supporting Information S1).

Taken together, these results suggest a warmer-than-PI Miocene climate across Europe, in a good agreement with temperature estimates derived from fossil flora. The experiment with higher pCO_2 (Mio_450) shows better agreement. Different Alpine elevations contribute to temperature changes restricted to the Alpine region and a different land-sea distribution in Europe has only minor effects on the regional temperature pattern.

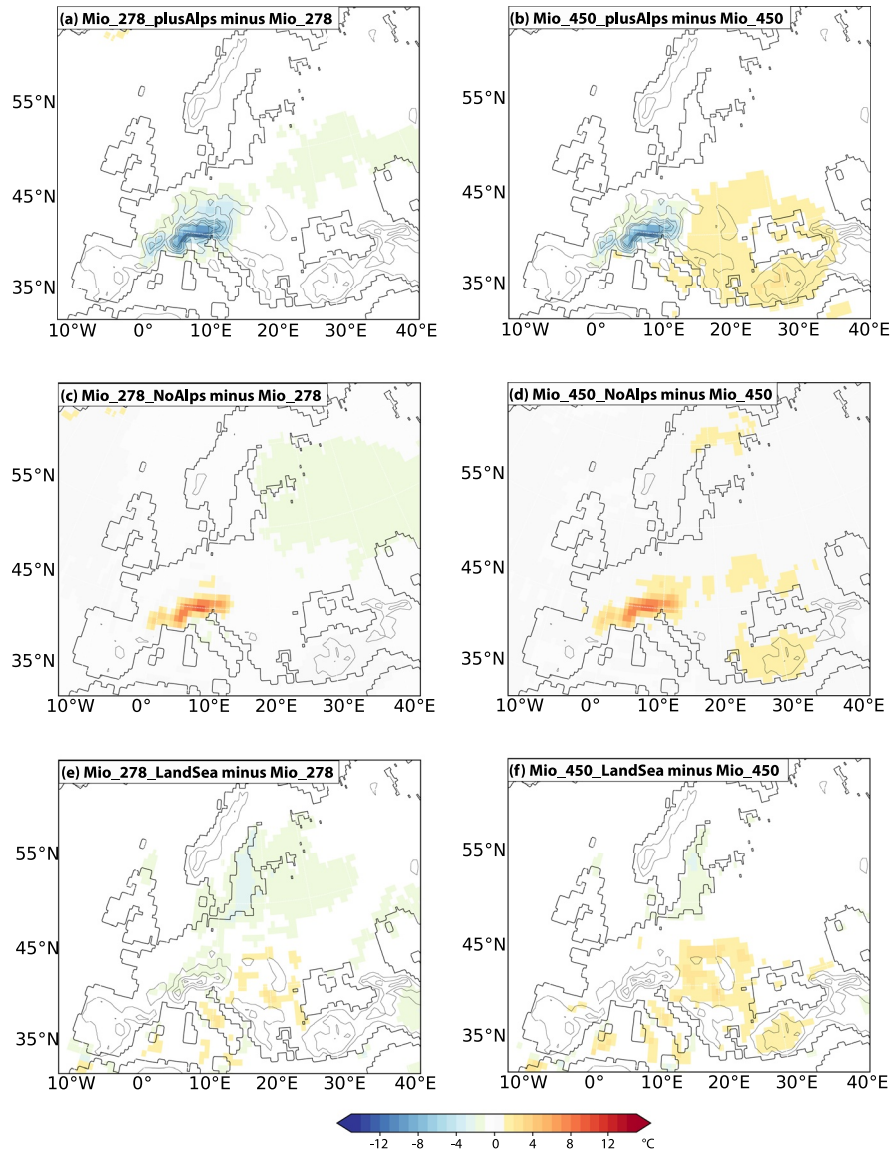

Figure 3. Temperature (at 2 m) change for the following simulation comparisons: (a) Mio_278_plusAlps relative to Mio_278, (b) Mio_450_plusAlps relative to Mio_450, (c) and Mio_278_noAlps relative to Mio_278, (d) Mio_450_noAlps relative to Mio_450, (e) Mio_278_LandSea relative to Mio_278, and (f) Mio_450_LandSea relative to Mio_450.

4.3. ECHAM5-Wiso Simulated Middle Miocene MAP

Simulations predict lower MAP for both Mio_278 and Mio_450 experiments than for PI over most of Western and Southern Europe (compare Figures 4c and 4d–4f). Meanwhile, an increase of 50–400 mm/yr is simulated for the MAP over Scandinavia and northwestern Russia. On average, for central Europe and the Alpine region, MAP for both the Mio_278 run and the Mio_450 run is less than for the PI (Table S4 in Supporting Information S1). Over the European Alps, MAP decreases across both the low-elevations and the high-elevation regions in both Miocene experiments compared to PI (Figures 4b–4d).

Investigation of the paleobotanic proxy data indicates larger precipitation amounts than predicted in the Mio_278 and Mio_450 experiments (Figure 4g; Table S5 in Supporting Information S1). However, the simulated MAP in the Mio_278 and Mio_450 runs is consistent with precipitation estimates from the ecophysiological structure of herpetological assemblages (herpetofaunal fossils; Figure 4h; Table S5 in Supporting Information S1).

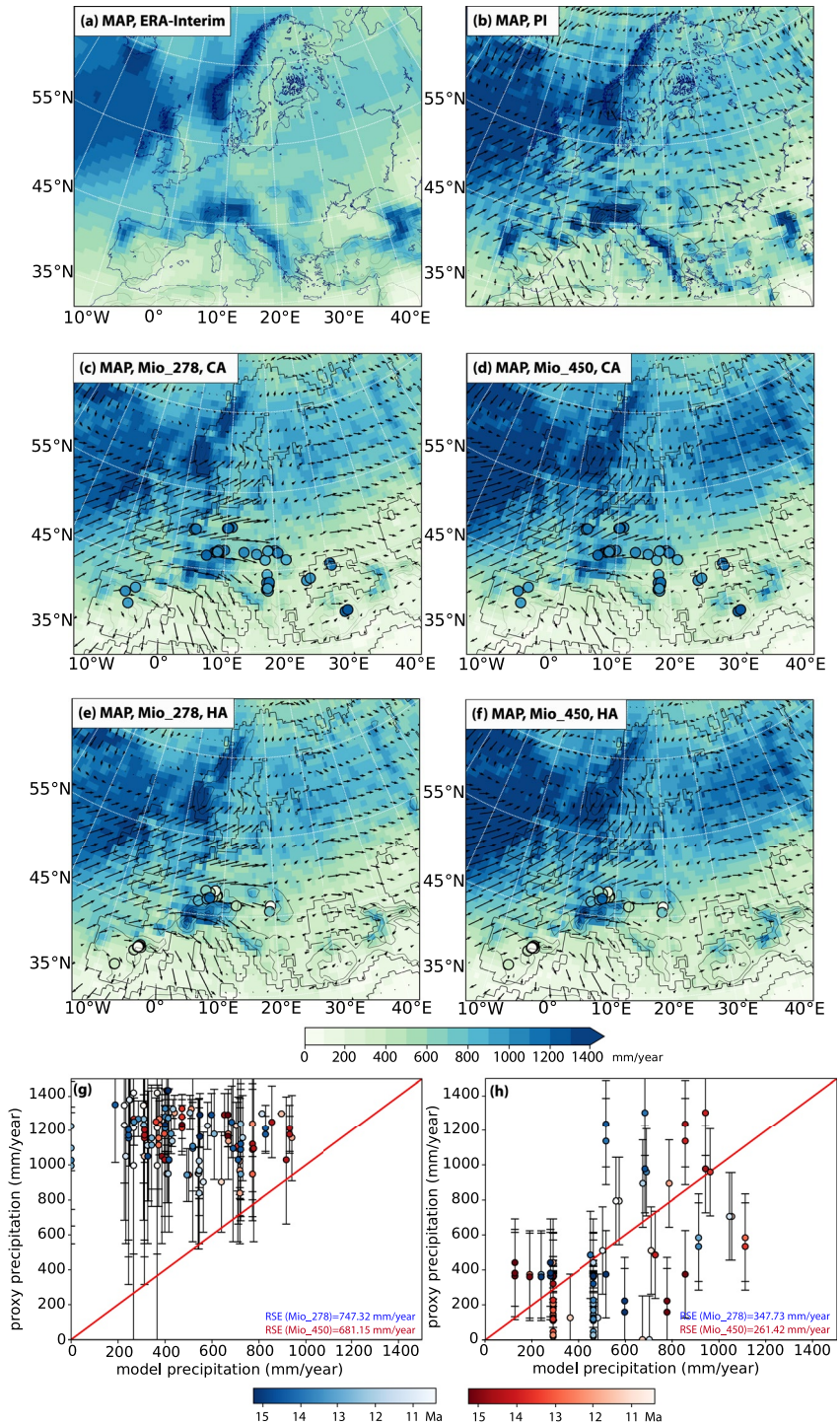

Figure 4. Mean annual precipitation (MAP) and mean annual winds at 10 m for ERA-Interim reanalysis (a) and ECHAM5-wiso experiments (b–f). (b) PI, (c, e) Mio_278, and (d, f) Mio_450 simulations. Vectors show near-surface winds. In subplots (c and d), the shaded circles show Middle Miocene MAP (as the mean between MAP max and MAP min correspondingly) reconstructed from fossil plant data using the coexistence approach (CA see Table S1). In subplots (e and f), the shaded circles show Middle Miocene MAP, reconstructed from the ecophysiological structure of the herpetological assemblages (HA; see Table S2). Subplot (g) shows the model MAP vs. MAP, reconstructed using the plant coexistence approach, subplot (h) shows the model MAP vs. MAP, reconstructed from the ecophysiological structure of the herpetological assemblages. The bluish colors for the points on subplots (g, h) correspond to the Mio_278 experiment and the reddish colors to the Mio_450 experiments. For the comparison with the two simulations, the corresponding data of all available ages are taken from Table S1 (g) and from Table S2 (h). The bluish colors show all points data when compared to the Mio_278 precipitation and the reddish colors—to the Mio_450 precipitation. Color intensity corresponds to the averaged absolute age of the data point (see Tables S1 and S2): light blue and light red—younger age, dark blue and dark red—older age. The red line shows a 1:1 model-data fit. Points restored to their paleo coordinates by means of GPLATES online tool (http://portal.gplates.org/service/).

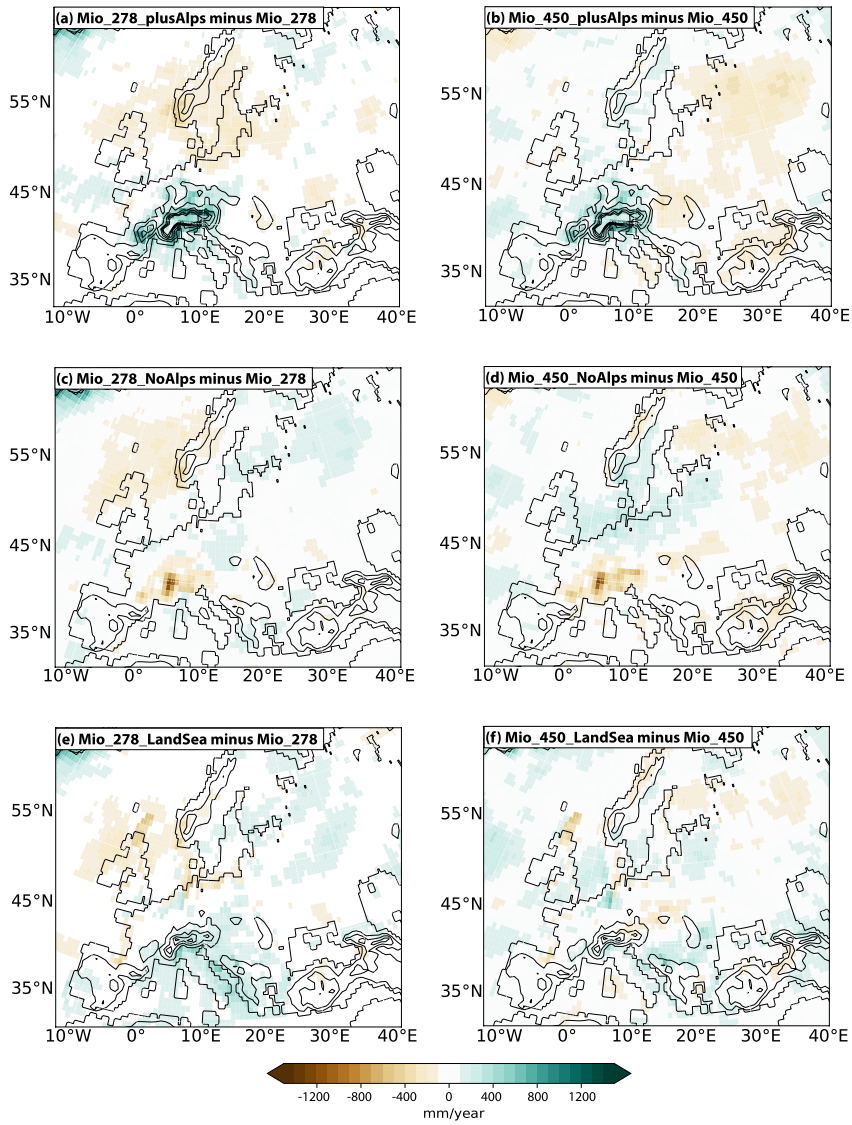

Figure 5. Precipitation change for (a) Mio_278_plusAlps relative to Mio_278, (b) Mio_450_plusAlps relative to Mio_450, (c) Mio_278_noAlps relative to Mio_278, (d) Mio_450_noAlps relative to Mio_450, (e) Mio_278_LandSea relative to Mio_278, and (f) Mio_450_LandSea relative to Mio_450.

Surface uplift of the Alps has both a regional and a far-field impact on European precipitation: with mountain growth, precipitation increases over the Alps and precipitation decreases across Eastern Europe (Figures 5a–5d). On average, experiments with higher Alpine elevation (Mio_278_plusAlps, Mio_450_plusAlps) suggest a precipitation increase by 141 and 57.2 mm/yr, respectively, for central Europe compared to the Mio_278 and Mio_450 simulations, respectively (Table S4 in Supporting Information S1). This increase is the most pronounced for the high-elevation region of the Alps. In contrast, experiments with reduced Alpine elevation (Mio_278_noAlps, Mio_450_noAlps) show a decrease in precipitation, which is most prominent over the high-elevation region. The precipitation change in the Mio_278_LandSea and Mio_450_LandSea simulations relative to the Mio_278 and Mio_450 runs, respectively is below 130 mm/yr over regions adjacent to the Alps (Figures 5e and 5f; Table S4 in Supporting Information S1). Higher changes in precipitation, up to 400 mm/yr, are simulated only for regions adjacent to the Paratethys Sea.

In summary, the key feature identified for the Miocene is a "bi-directional" precipitation change compared to PI conditions: an increase in precipitation over Scandinavia and Northern Europe and a decrease in precipitation over central Europe, Southern Europe, and the Mediterranean. Increased surface elevation of the Alps leads to

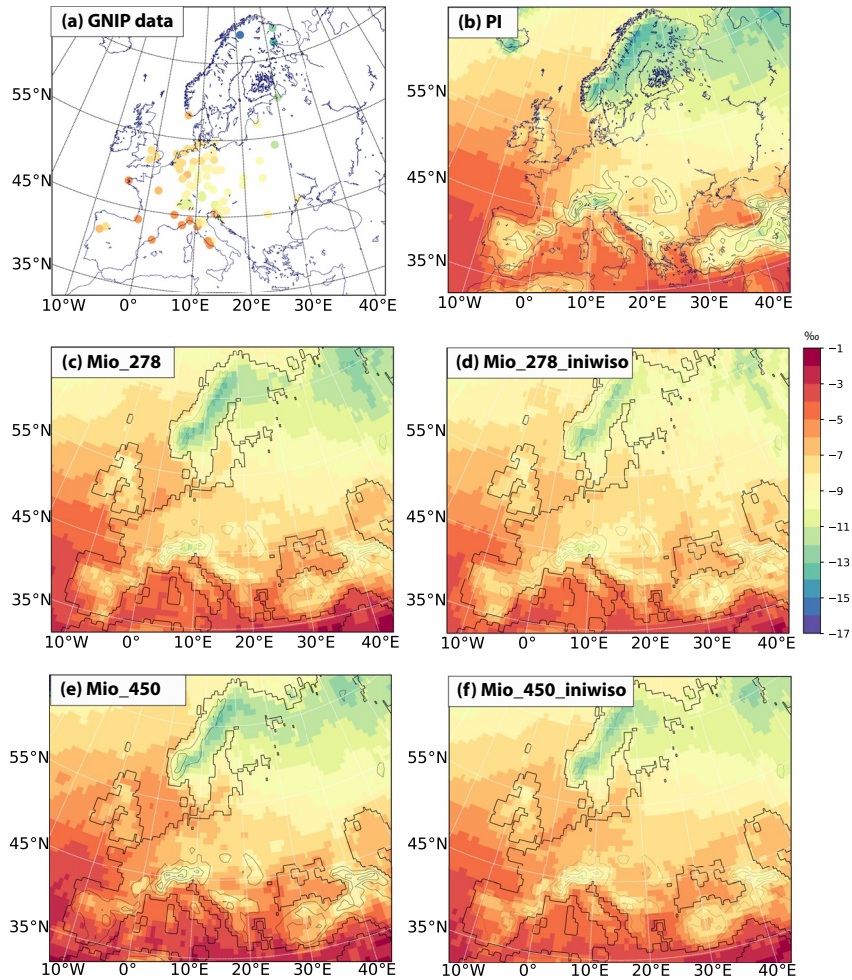

Figure 6. Annual mean $\delta^{18}O_p$ from the International Atomic Energy Agency (IAEA) Global Network of Isotopes in Precipitation (GNIP) observations (a) and ECHAM5-wiso simulated annual mean $\delta^{18}O_p$ values for: (b) the PI, (c) the Mio_278, (d) Mio_278_iniwiso, (e) the Mio_450, and (f) Mio_450_iniwiso experiment.

increased orographic precipitation rates restricted to the Alps region, with most prominent changes over Alpine high elevations. Simulated precipitation rates for both pCO_2 setups are consistent with precipitation estimates from the ecophysiological structure of herpetological assemblages. However, MAP estimates based on the coexistence approach exceed those from the herpetological assemblages and the Miocene model results.

4.4. ECHAM5-wiso Simulated Middle Miocene Mean Annual $\delta^{18}O_p$

The simulated mean annual $\delta^{18}O_p$ patterns for both the Mio_278 and the Mio_450 experiments are qualitatively similar to the predicted PI $\delta^{18}O_p$ pattern across Europe. Predicted $\delta^{18}O_p$ values generally decrease from south to north, from continental margins to the continental interior and from low-to high-elevation regions (Figure 6; Figure S4 in Supporting Information S1). The most negative values are simulated over Scandinavia, NW Russia, and the Alps. The average annual $\delta^{18}O_p$ value for central Europe and the Alpine region in the Mio_278 and Mio_450 simulations is 0.5‰ and 1‰ higher than in the PI, respectively (Table S4 in Supporting Information S1). Averaged over the low-elevation region, $\delta^{18}O_p$ is 0.6‰ higher for Mio_450 than for the PI, while Mio_278 is approximately the same as in the PI. For the high-elevation region, the mean $\delta^{18}O_p$ value is 0.7‰ (Mio_278) and 1.5‰ (Mio_450) higher than for the PI. Our simulations with modified seawater $\delta^{18}O$ (Mio_278_iniwiso and Mio_450_iniwiso) show low sensitivity of the $\delta^{18}O_p$ over central Europe to this parameter (Figure 6; Table S4 in Supporting Information S1).

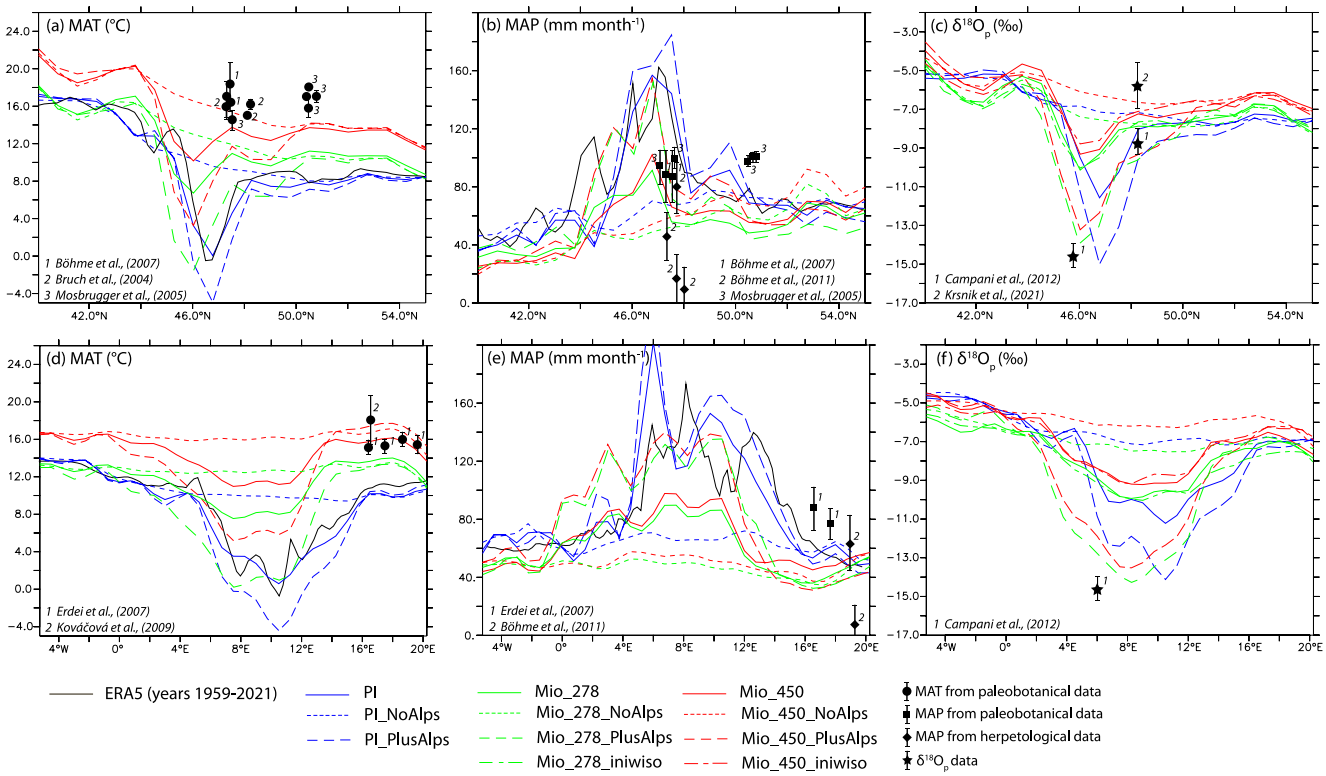

Figure 7. Annual mean temperature (a, d), precipitation (b, e), and $\delta^{18}O_p$ (c, f) gradients across the Alps: (a–c) averaged between 9°E and 10°E and (d–f) between 46°N and 47°N for topographic sensitivity experiments with pre-industrial (PI_NoAlps, PI, PI_plusAlps) and Middle Miocene (Mio_278, Mio_450, Mio_278_noAlps, Mio_450_noAlps, Mio_278_plusAlps, Mio_450_plusAlps, Mio_278_iniwiso, Mio_450_iniwiso) boundary conditions and for ERA5 reanalysis time averaged from 1959 to 2021. Selected data points (for MAT [Table S1], MAP [Table S1 and Table S2], and $\delta^{18}O_p$ [Campani et al., 2012; Krsnik et al., 2021]) between 8°E and 11°E (a–c) and between 45°N and 49°N (d–f) extrapolated to the section line are shown in black.

Over the Alps, the $\delta^{18}O_p$ values for the PI show a clear decrease from the foothills to the summit across both South-North (averaged between 9°E and 10°E) and East-West (averaged between 46°N and 47°N) profiles (Figures 7c and 7f). For the PI simulation this change is −0.25‰/100 m in the Northern Alps for annual mean values, which is consistent with the modern precipitation-weighted isotopic lapse rate (−0.2‰/100 m in the Northern Alps; Campani et al., 2012) and close to the empirically determined global river-based average of (−0.28 ‰/100 m; Poage & Chamberlain, 2001). For both Mio_278 and Mio_450 experiments the annual mean isotopic lapse rate along the North Alpine flank is −0.2‰/100 m.

In the experiments with increased topography (Mio_278_plusAlps and Mio_450_plusAlps) $\delta^{18}O_p$ values are on average 2.3‰ and 3.0‰ lower than in the Mio_278 and Mio_450 simulations over the high-elevation region (Figure 8; Figure S4 in Supporting Information S1; Table S4 in Supporting Information S1). The maximum changes are −5.3% and −5.8‰ for the Mio_278_plusAlps minus Mio_278 and Mio_450_plusAlps minus Mio_450, respectively, for high-elevation region. The differences between these simulations are within 0.6‰ for the central Europe region and for the low-elevation region. In experiments with reduced topography (Mio_278_noAlps and Mio_450_noAlps) $\delta^{18}O_p$ values are on average 1.5‰ and 1.3‰ higher relative to Mio_278 and Mio_450, respectively. Note that the maximum change in $\delta^{18}O_p$ values occurs over the highest Alpine topography, while over the foothills the magnitude of the difference between experiments with modern and modified topography is within 1–2‰ (Figure 7).

Taken together, our predicted mean annual $\delta^{18}O_p$ values differ by less than 1.5‰ from the PI mean annual $\delta^{18}O_p$ values for both pCO_2 setups in the Miocene. Removal of Alpine topography contribute to an increase in $\delta^{18}O_p$ of up to 5.8‰ relative to the Miocene experiment with 100% of the Alps topography and up to 8‰ relative to an experiment with doubling of Alpine topography. Warmer Miocene climate contributes almost imperceptibly (0.03‰/100 m) to shallowing of the oxygen isotope lapse rate at annual scale. In the following, we investigate seasonal variations of selected variables in order to better understand seasonal bias in annual-mean values.

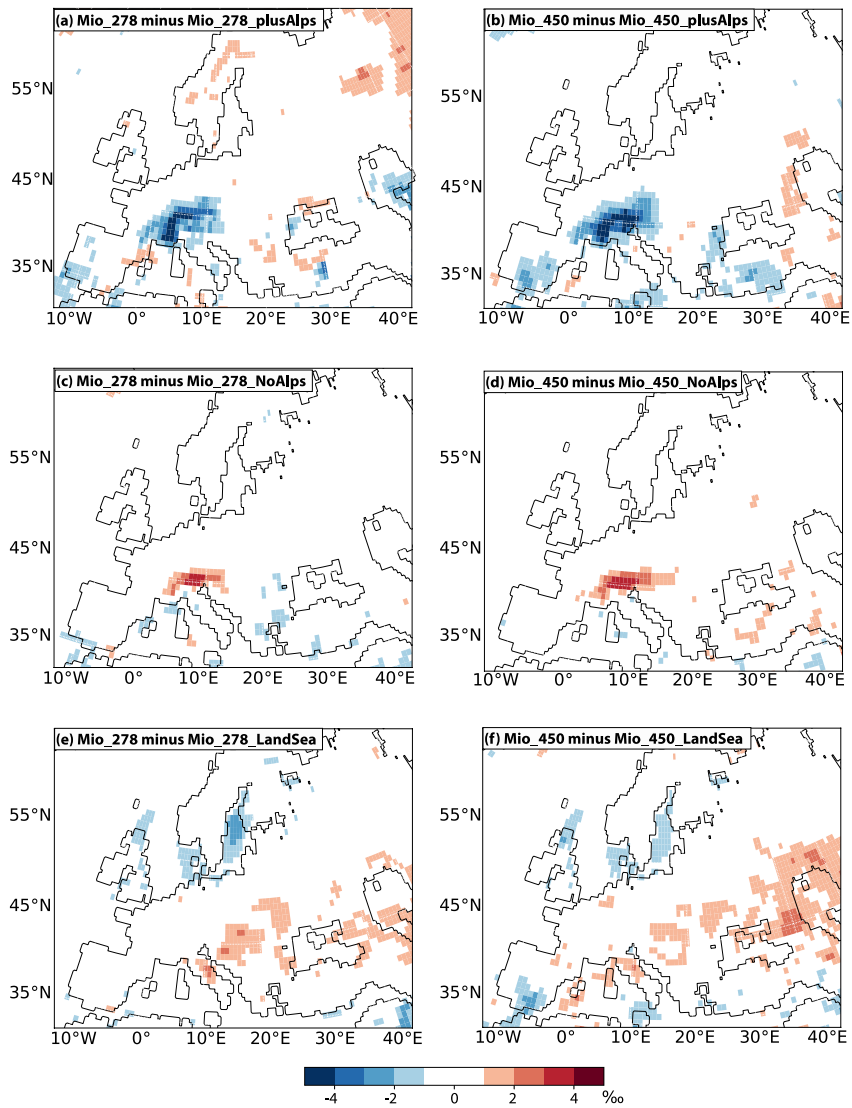

Figure 8. Stable oxygen isotopes change for (a) Mio_278_plusAlps relative to Mio_278, (b) Mio_450_plusAlps relative to Mio_450, and (c) Mio_278_noAlps relative to Mio_278, (d) Mio_450_noAlps relative to Mio_450, (e) Mio_278_LandSea relative to Mio_278, and (f) Mio_450_LandSea relative to Mio_450.

4.5. Seasonality of Temperature, Precipitation, Relative Humidity, Evaporation, $\delta^{18}O$ in Vapor and $\delta^{18}O$ in Precipitation

In this section, we report intra-annual variations in simulated near-surface temperature, precipitation, evaporation, near-surface relative humidity, $\delta^{18}O_v$ and $\delta^{18}O_p$ values, averaged over central Europe and the Alpine region (Figure 9). The same variables averaged for the low-elevation region and for the high-elevation region (regions as shown in Figure 2a), are shown in Figures S5 and S6 in Supporting Information S1. We also compare the simulated seasonality of temperature and precipitation with seasonal temperature and precipitation signals derived from proxy data (CMT, WMT, HMP, LMP). We present the intra-annual variations in temperature, precipitation, evaporation and near-surface relative humidity to explain simulated $\delta^{18}O_v$ and $\delta^{18}O_p$ signals.

4.5.1. Near-Surface Temperature

The seasonal cycles of near-surface temperature in Mio_278 and Mio_450 simulations are similar to those in the PI. The minimum monthly mean temperature (CMT) is simulated in January for PI, Mio_278, and Mio_450 and a maximum monthly mean temperature (WMT)—in July for PI and Mio_273 and in August for Mio_450

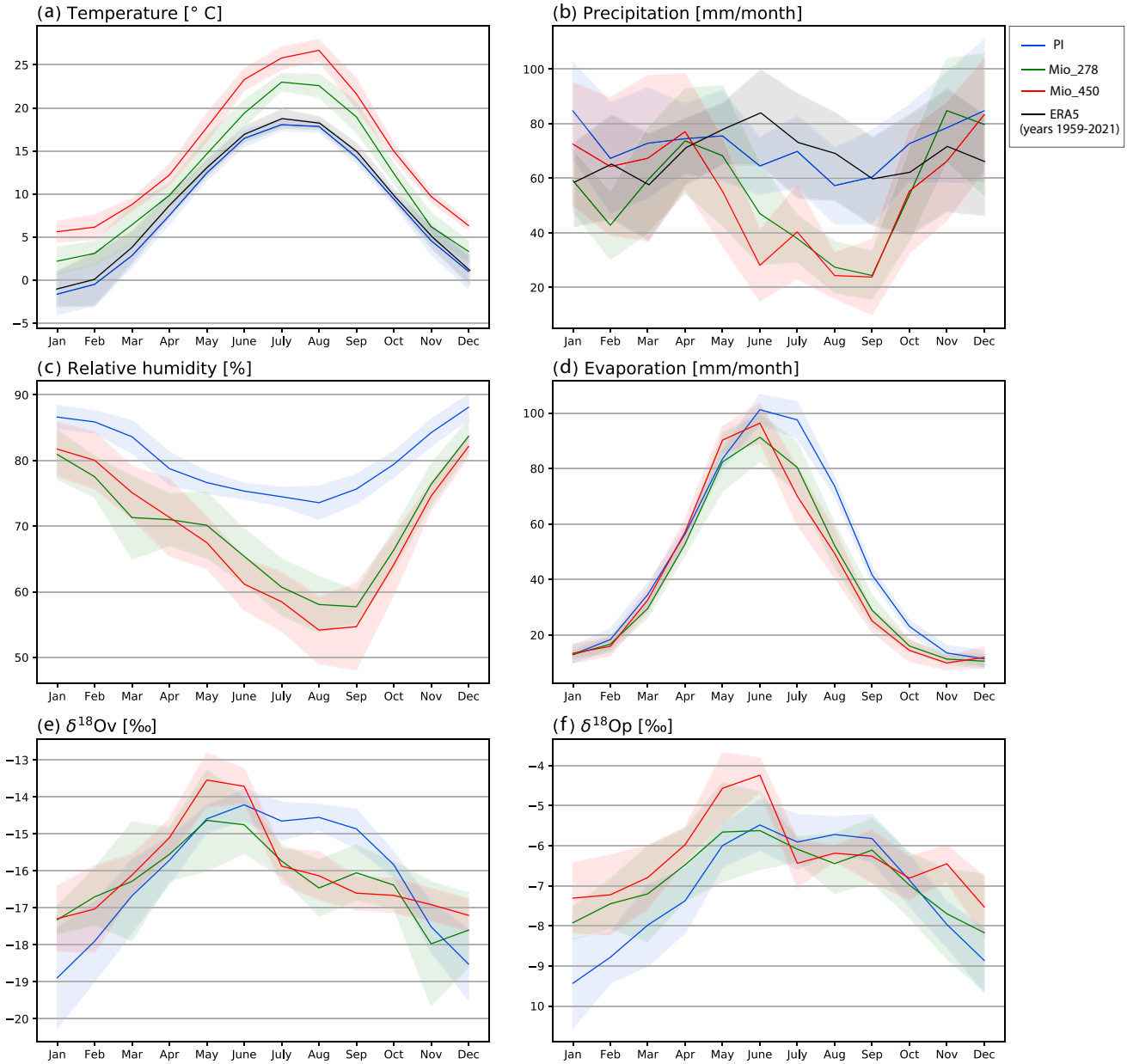

Figure 9. Intra-annual variations of (a) near-surface temperature, (b) total precipitation, (c) low-level relative humidity, (d) surface evaporation, (e) $\delta^{18}O_v$ values, and (f) $\delta^{18}O_p$ values. All variables are averaged for continental central Europe. Blue color corresponds to the PI experiment, green—Mio_278 experiment, red—Mio_450 experiment, black—ERA5 reanalysis from 1959 to 2021. Solid lines show multi-annual mean, shade shows interannual variability within one standard deviation for the corresponding variable.

(Figure 9a). However, the mean annual range of temperature increases in Miocene relative to PI (Table S4 in Supporting Information S1). Both Mio_278 and Mio_450 experiments show agreement with the data from the coexistence approach in WMT (RSE is 3.8°C and 5.4°C, respectively; Figures 2e and 2f; Table S5 in Supporting Information S1). The Mio_278 experiment shows a lower fit to CMT derived from proxy data, with RSE values of 4.7°C, while the Mio_450 experiment shows a better fit of 4.4°C. The best fit in the WMT and the CMT is found for the sites located in Southern Europe (Figure S7 in Supporting Information S1).

4.5.2. Precipitation

Results indicate December as the month with the highest monthly precipitation (HMP) for PI, Mio_278, and Mio_450; the driest month (LMP) is August for PI and September for Mio_278 and Mio_450 (Figure 9b). The

precipitation seasonality over central Europe increases in the Miocene simulations compared to the PI simulation. For January, February, and March precipitation is similar in the PI and Mio_450 simulations, whereas there is slightly less precipitation in the Mio_278 experiment. However, the summer months (from May to October) are drier in the Mio_278 and Mio_450 simulations compared to the PI. The November and December precipitation is again similar in the PI, Mio_278, and Mio_450 simulations.

When compared to fossil plant data, both the Mio_278 and Mio_450 simulations have a low fit for HMP (RSE is 54.7 mm/month and 33.6 mm/month, respectively) and LMP (RSE = 37.0 mm/month for Mio_278 and RSE = 37.7 mm/month for Mio_450) (Table S5 in Supporting Information S1; Figure S8 in Supporting Information S1).

4.5.3. Relative Humidity

For the PI simulation, the relative humidity reaches its maximum of 88% in December and its minimum of 73% in August (Figure 9c). The seasonal cycle is different in simulations Mio_278 and Mio_450 relative to the PI. While winter values are slightly lower in the Miocene simulations, in summer months a significant drop of humidity is predicted, with the maximum decrease occurring for August–September. The difference in relative humidity between the Mio_278, Mio_450, and PI results is 8%–12% for May–June and 18%–20% for August–September.

4.5.4. Evaporation

For PI the maximum evaporation (100 mm/month) occurs is in June and July, with a gradual decrease starting in August toward its yearly minimum (14 mm/month) in November and December (Figure 9d). The peak in annual evaporation for both Mio_278 and Mio_450 simulations is in June, with a continuous decrease toward the yearly minimum in November (12 and 13 mm/month, respectively) starting in July.

4.5.5. $\delta^{18}O$ in Vapor, $\delta^{18}O$ in Precipitation

For the PI simulation both the $\delta^{18}O_v$ and $\delta^{18}O_p$ have minimum values in January (−18.9‰ for $\delta^{18}O_v$ and −9.4‰ for $\delta^{18}O_p$). The values then increase from February to June, toward their maximum in June (−14.2‰ for $\delta^{18}O_v$ and −5.5‰ for $\delta^{18}O_p$). From midsummer to September relatively high values occur with a subsequent smooth decrease starting in October (Figures 9e and 9f). Intra-annual variations in $\delta^{18}O_v$ and $\delta^{18}O_p$ for the Mio_450 simulation are different from the PI, while $\delta^{18}O_v$ and $\delta^{18}O_p$ values of the Mio_278 simulation are different from those of the PI only for November–April, but largely overlap with PI during May–October. For example, minimum $\delta^{18}O_v$ and $\delta^{18}O_p$ occur in December with values of −17.6‰ for $\delta^{18}O_v$ in the Mio_278 and −17.2‰ in the Mio_450 simulations, and −8.1‰ and −7.5‰ for $\delta^{18}O_p$ for the Mio_278 and the Mio_450. Maximum values are predicted for May and June (−14.6‰ and −13.5‰ for $\delta^{18}O_v$ for Mio_278 and Mio_450, respectively; −5.6‰ and −4.2‰ in $\delta^{18}O_p$ for Mio_278 and Mio_450, respectively) with an abrupt decrease in July.

In summary, the seasonal cycle of $\delta^{18}O_v$ and $\delta^{18}O_p$ values differs between PI and Miocene simulations, but are similar between the two Miocene simulations. Thus, changes in Miocene CO_2 concentration have less impact on the seasonality change in $\delta^{18}O_v$ and $\delta^{18}O_p$.

4.6. SLP Shifts

We analyzed sea-level pressure shifts for February–March, May–June, August–September, and November–December. We chose these months rather than "classic" seasons (e.g., December–January–February or June–July–August), because we aim to explain the previously described $\delta^{18}O_p$ changes, which are most pronounced for these months (Figure 9). In February–March, we find an increase in sea-level pressure over Turkey, Italy and the Balkans, with a maximum increase of 3 and 1 hPa over Italy for the Mio_278 and Mio_450 simulations, respectively (Figures 10a and 10b; Figure S9 in Supporting Information S1). This sea-level pressure increase is accompanied by a sea-level pressure decrease over the North Atlantic (from 20°W to 0° and 45°N to 65°N) up to 6 hPa in both cases. In May–June and August–September, the sea-level pressure for both the Mio_278 and Mio_450 simulations is lower than in the PI simulation (Figures 10c and 10f). The most pronounced changes (>10 hPa) for these months occur over Northeast Africa, the Red Sea, and the North Atlantic, while the sea-level pressure change over central Europe is smaller, ranging from 3 to 5 hPa. For November-December, the high Miocene SLP remains over Southern Europe, with a maximum increase of 1 and 3 hPa for the Mio_278 and Mio_450 simulations, respectively (Figures 10a and 10b).

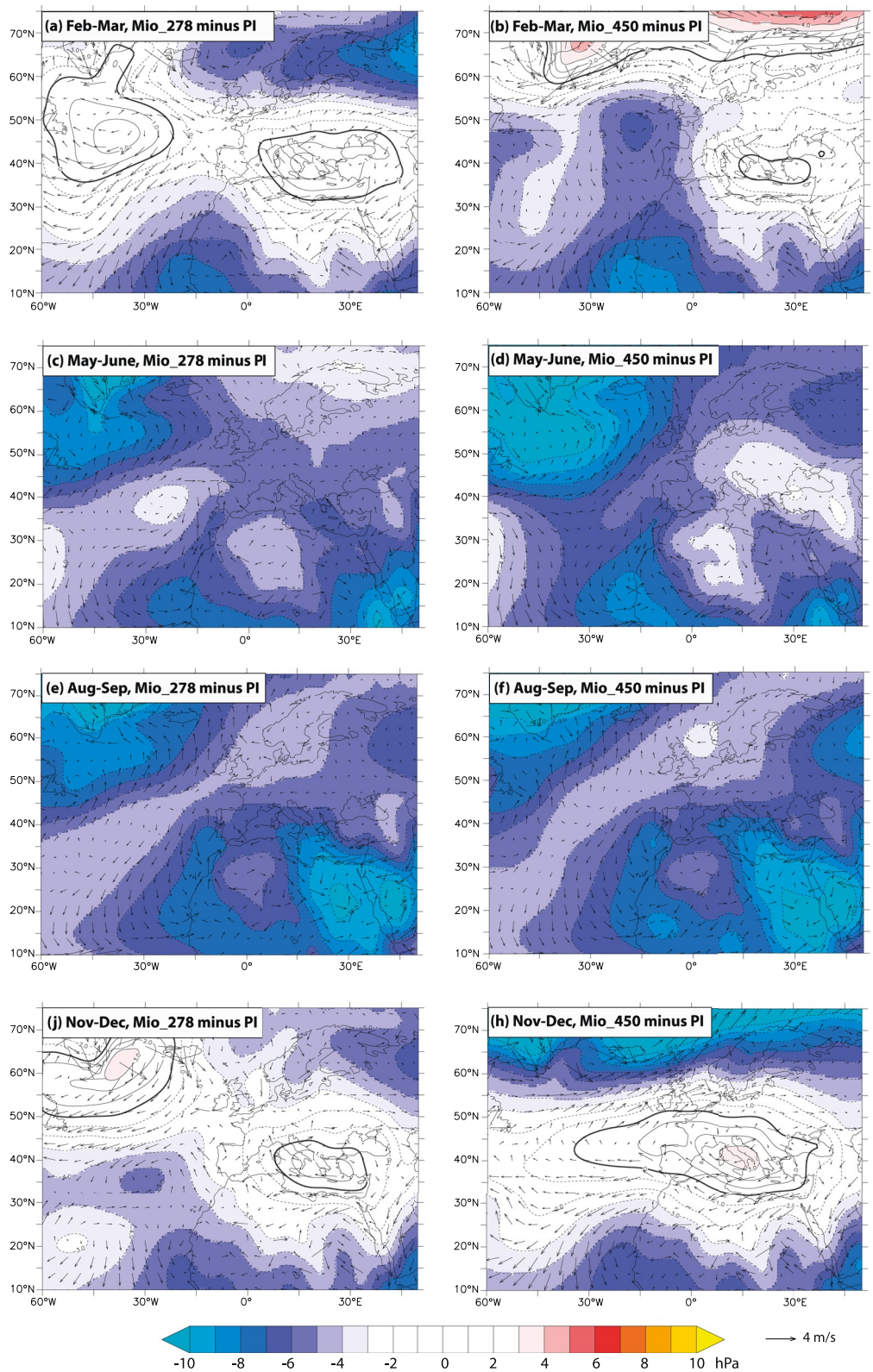

Figure 10. Differences in the mean sea level pressure (SLP) and winds between Mio_278 and PI (a, c, e, j) and between Mio_450 and PI (b, d, f, h) simulations averaged over selected months: February–March (a, b), May–June (c, d), August–September (e, f), November–December (j, h). The isolines show the SLP difference with an interval of 1 hPa; the black solid line corresponds to zero difference.

5. Discussion

In the following sections, we provide explanations for the simulated humidity and precipitation change in the Middle Miocene compared to the PI (Section 5.1). Following this, we assess the potential sources of model-data mismatch in terms of precipitation by comparing the fit of climatic conditions based on different proxy-data reconstruction methodologies to those derived from our model outputs (Section 5.2). In Section 5.3, we explain the simulated $\delta^{18}O_p$ on annual and intra-annual scale and examine the impact of global and regional Middle Miocene climate change that is linked to Alpine surface uplift and Paratethys retreat on carbonate $\delta^{18}O$ records. In Section 5.4, we conclude by discussing the consequences of these results for stable isotope paleoaltimetry studies.

5.1. Large-Scale Drivers of Humidity and Precipitation Change in Europe

For the Middle Miocene we simulate a bi-directional precipitation change pattern in Europe. More specifically, Scandinavia and northern Russia become wetter, while Southern and South-Eastern Europe become drier. This pattern persists for all seasons, but is most pronounced for late summer (Figures 11a–11c). This Middle Miocene bi-directional precipitation change in Europe is similar to the precipitation trends over the past century and the model predictions for future climate from Knutti and Sedláček (2013) and the Fifth Assessment Report of the Intergovernmental Panel on Climate Change (IPCC, 2013). The similarity between precipitation changes during the Middle Miocene (independent of CO_2 levels) and future climate is consistent with the idea that past warm climates represent analogs for the future climate and can anticipate how European precipitation might respond to global warming. In the following, we discuss possible driving mechanisms for changes in precipitation and humidity in Middle Miocene Europe.

In our Middle Miocene simulations, an anticyclonic circulation is centered over the Mediterranean and Southern Europe in winter (Figures S9k–S9m in Supporting Information S1). In addition, the Icelandic Low gets stronger during summer months (Figures S9d–S9j in Supporting Information S1) and promotes a northward shift of the Atlantic storm track with a deflection of storms north of the Mediterranean to higher latitudes. This mechanism has also been predicted for future climate change in Europe, according to Giorgi and Lionello (2008), who also note that increased high pressure and anticyclonic conditions generally lead to greater atmospheric stability and thus less favorable conditions for storm generation. As a result of these circulation changes, Southern Europe and the Mediterranean region show a general decrease in precipitation in the Middle Miocene, while the northern European regions show an increase.

Anticyclones are generally associated with atmospheric subsidence. During the modern summer, the Mediterranean is directly under the descending branch of the Hadley circulation which is caused by deep convection in the tropics (Lelieveld et al., 2002). Our Middle Miocene simulations show an extended area of positive vertical velocity (ω) over the eastern Mediterranean and the Balkans (Figures 11h and 11j; Figures S11h and S11j in Supporting Information S1), which is a direct indication of subsiding air masses. Compared to the PI (Figure S11g in Supporting Information S1), this area of positive ω is larger, especially for late summer, and extends toward central Europe and the Alps (Figures 10g–10j). This large-scale subsidence from upper to lower troposphere during the Middle Miocene, accompanied by advection and limited divergence for the largest part of the tropospheric column, explains the descending relative humidity structures and the dry surface hydroclimate. Sustained subsidence aloft, combined with a cool lower-level marine flow, results in a semi-permanent inversion that suppresses vertical growth of low clouds, and hence inhibits precipitation (Saaroni & Ziv, 2000).

The enhanced subsidence could possibly be related to the remote forcing of tropical circulation. Both the Asian summer monsoon (Rodwell & Hoskins, 2001; Tyrlis et al., 2013; Ziv et al., 2004) and the West African monsoon (Gaetani et al., 2011) have been suggested to influence the subsidence in the Mediterranean region. Rodwell and Hoskins (2001) demonstrated that the diabatic heating in the Asian monsoon region can induce a Rossby wave pattern to the west. They also found that the interaction between the Rossby waves and the mid-latitude westerlies produces an adiabatic descent over the Mediterranean and the subtropical Atlantic Ocean. Gaetani et al. (2011) reported a strong link between the summer Euro-Atlantic circulation and the convective activity of the West African monsoon. They show that the intensification of the Azores High, the northward shift of the West African Intertropical Convergence Zone and a Rossby wave from tropical America have a direct impact on the Euro-Atlantic circulation subsidence pattern. A detailed analysis of the causes of the subsidence change in the Middle Miocene would certainly be worthwhile, but is beyond the scope of this paper.

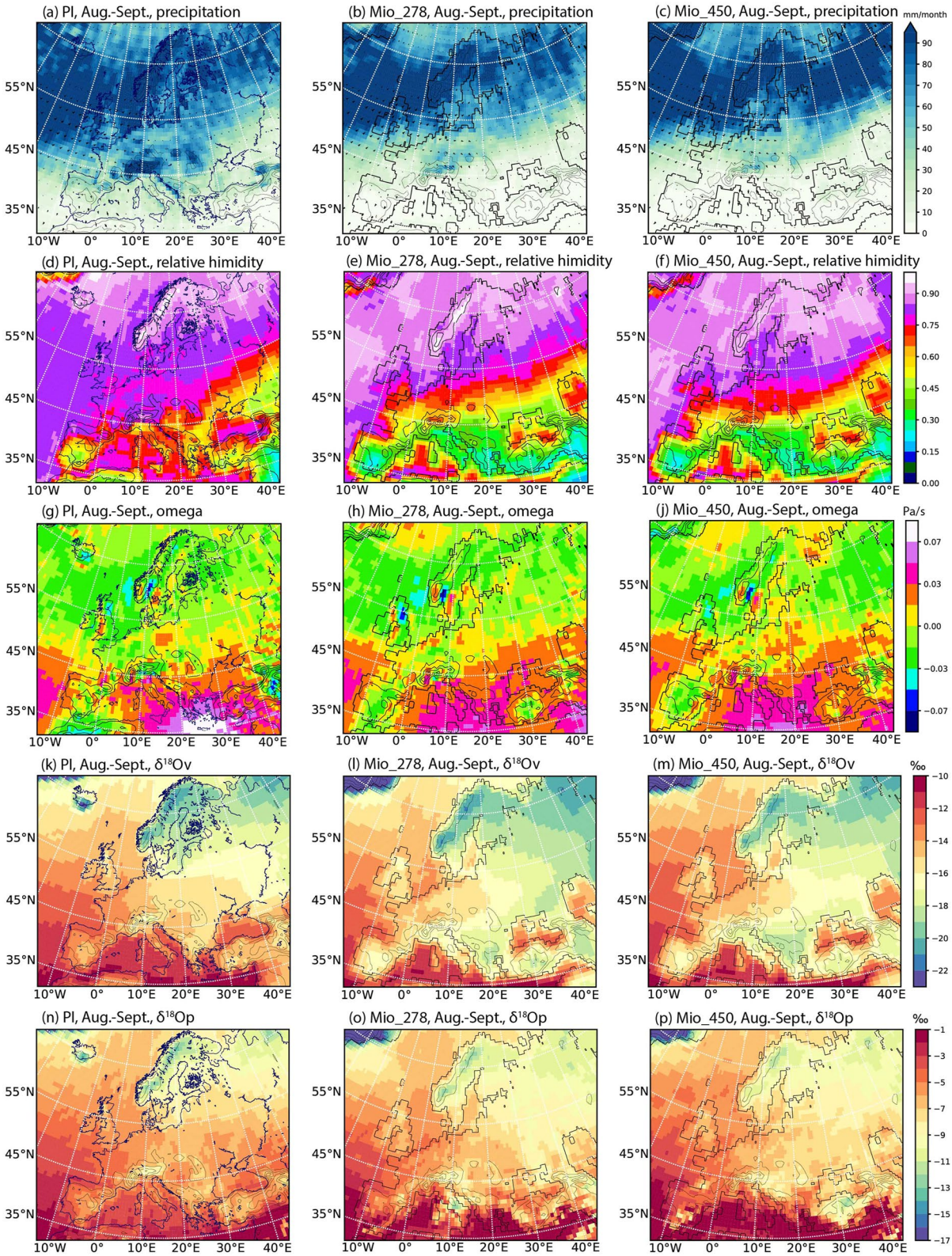

Figure 11. Precipitation amount (a–c), relative humidity (d–f), vertical velocity (omega) at 500 hPa (g–j), $\delta^{18}O_v$ (k–m), and $\delta^{18}O_p$ (n–p) for PI (a, d, g, k, n), Mio_278 (b, e, h, l, o), Mio_450 (c, f, j, m, p) simulations. Variables averaged for August–September.

In addition to the enhanced subsidence, reduced moisture transport from the Northern Atlantic, low precipitation rates and low relative humidity in Southern Europe (Figure S10 in Supporting Information S1) could be further amplified by reduced land evaporation and precipitable water. A reduction in precipitation leads to a depletion of soil moisture, which reduces the contribution of land evaporation to precipitable water, further reducing the precipitation simulated in our Middle Miocene experiments.

5.2. Wetter or Drier Europe in the Middle Miocene?

Our Middle Miocene control experiments (Mio_278 and Mio_450) show lower MAP for most parts of Central and Southern Europe than in the PI simulation. This is consistent with the results of Böhme et al. (2011), who suggest lower precipitation, up to 300–500 mm/yr less than today, for the Southwest (Calatayud-Teruel basin) and central Europe (Western and Central Paratethys) during the late Langhian (~14.40–13.65 Ma) and Serravallian (13.82–11.63 Ma). These results are also supported by the coeval occurrence of evaporites in the Spanish basins (Abdul Aziz et al., 2003). Moreover, abundant soil carbonate formation in the North Alpine Molasse basin during the Middle Miocene (Campani et al., 2012; Krsnik et al., 2021; Methner et al., 2020; Schlunegger et al., 2007) indicate precipitation rates not higher than 800 mm/yr (Breecker et al., 2009) or even 500 mm/yr (Zamanian et al., 2016) as well as pronounced precipitation seasonality. However, these reconstructions, taken together with our modeling results and herpetological proxy estimates, are at odds with plant proxy data showing wetter than present conditions in Central and Eastern Europe during the Serravallian (~13.8 to ~11.6 Ma; Bruch et al., 2011), with precipitation rates of up to 1,400 mm/yr. The paleobotanical data come from more than a dozen different authors and papers (Table S1), whereas the herpetological data come from only from two publications (Table S2). Nevertheless, all paleobotanic papers use the same method (Mosbrugger & Utescher, 1997) and the same reference for the Nearest Living Relative (NLR) of a fossil taxon, that is, they are internally consistent as are the herpetofaunal data. The discrepancies between the paleobotanical records and other geologic proxies as well as our modeling can be explained by: (a) difficulties in reconstructing dry climates with botanical methods; (b) uncertainties linked to the coexistence approach; and (c) climate model-related uncertainties.

First, problems arising when reconstructing dry conditions from plant fossils are already well known (e.g., in Böhme et al., 2007, 2011; Bruch et al., 2011). Ultimately, the lack of fossil floras preserved under dry conditions leads to a strong bias in the data with gaps toward southern Europe, where plant proxy data are only available from wetter regions of Spain (North-East coast) and northern Italy (Bruch et al., 2011). Moreover, faunal and floral remains from Central and Eastern Europe usually come from different stratigraphic levels and taphonomic settings (Bruch et al., 2011). This could mean that paleobotany proxy data do not have the necessary resolution and taphonomic capability to detect dry climates. On the other hand, the formation of carbonates can occur under overall (annual) rather wet conditions as long as a necessary precipitation seasonality is given. For instance, pedogenic carbonates are known to form under monsoonal climate (Breecker et al., 2009; Quade et al., 2007). As such, pedogenic carbonates can inherit a strong seasonal bias (e.g., Kelson et al., 2020).

Second, most botanical paleoclimate data are derived from the coexistence approach (Mosbrugger & Utescher, 1997). However, concern has been raised about the reliability of climate reconstructions, especially outside the warm-temperate climatic window (see Grimm & Denk, 2012 for detailed discussions). Moreover, the coexistence approach is strongly taxon dependent. In contrast, the herpetological method refers to the relative diversity (taxon count) of eco-physiologic groups of ectothermic animals at a given locality and is therefore largely taxon independent (especially below family levels). As highlighted earlier, the temperature records from palaeobotanical proxies are in a good agreement with the model, unlike the precipitation records. Further model simulations with regional geographic adjustments could help reconcile the herpetological data, botanical data, and modeling results.

Third, in terms of accurate simulation of paleoprecipitation, the application of ECHAM5-wiso has several limitations, related to (a) model resolution, (b) model parameterizations, for example, convective and evapotranspiration schemes, (c) no ocean feedback in an atmosphere-only GCM, (d) uncertainties in the choice of boundary conditions (e.g., vegetation, SSTs, etc.), (e) uncertainties in simulation of higher temporal and spatial scale atmospheric circulations (e.g., Shields et al., 2021), and (f) uncertainties in simulation equator-to-pole SST gradient (Burls et al., 2021). Compared to a coarse model resolution, for example, the experiments participating in MioMIP1 (T31 or T42, corresponding to a grid spacing of ~3.75° or ~2.79°, respectively), we find two dominant patterns

in which the ECHAM5-wiso simulations (T159 resolution, corresponding to a grid spacing of ~0.75°) differ: generally a cold bias over mountain ranges such as the European Alps, which could be related to differences in orography between low- and high-resolution models (with higher elevation in our high-resolution simulations), and a warm bias over the continents. Models with higher resolution have been shown to have higher climate sensitivity, but this effect is not present in all models (e.g., Ingram & Bushell, 2021 and references therein). Whether the higher climate sensitivity due to resolution contributes to the relative warmth over the continents needs further investigation based on additional simulations.

We refer the reader to Botsyun and Ehlers (2021) for a further discussion of the uncertainties relevant to precipitation and $\delta^{18}O_p$ values. In addition, major uncertainties are related to the choice of regional topographic configurations in Europe. Simulations with increased Alpine elevation suggest an increase in precipitation over the Alpine region and a better fit to paleobotany proxy data over these regions. However, for Spanish basins, the Pannonian Basin, the Carpathian region, Crimea, Romania, and Turkey, models with increased Alpine elevation still show lower precipitation amounts comparable to the prediction of the paleobotany data. In our simulations, however, we do not test different uplift scenarios for mountains other than the Alps in Europe or a differentiated uplift history of the Eastern and Western Alps, which could potentially lead to a redistribution of precipitation. Our model resolution is still not high enough to capture microenvironments existing along inland water bodies, which could harbor many flora and fauna species characteristic of wetter climates, even if overall larger scale climate is (sub-)arid. Moreover, such environments have high preservation rates, biasing geologic records toward sheltered locations (Chandler et al., 1992).

In summary, despite some model-related limitations, our modeling results, in accord with herpetological proxy estimates and geological observations (evaporites, soil carbonates) indicate lower than pre-industrial precipitation rates for Central and Southern Europe during the Middle Miocene. High precipitation rates predicted by the coexistence approach are not supported by the model results here.

5.3. Implications of Global Climate Change and Alpine Surface Uplift on Water Stable Isotope Records and Paleoclimate Proxy Records in Europe

Changes in terrestrial paleo-$\delta^{18}O_p$ patterns are typically linked to both mountain uplift and global climate change (Caves et al., 2015; Licht et al., 2014; Methner et al., 2020; Mulch, 2016; Quade et al., 2011). Isotope-enabled GCMs provide a tool for distinguishing the processes impacting $\delta^{18}O_p$ values at both regional and local scales (Botsyun & Ehlers, 2021). Comparing pre-industrial and Middle Miocene simulations (Mio_278 and Mio_450) allows us to isolate the effect of global climate on the $\delta^{18}O_p$ pattern in Europe. Further comparison of Middle Miocene simulations (Mio_278 and Mio_450) and simulations with a varied Paratethys Sea extent (Mio_278_LandSea and Mio_450_LandSea) allows us to isolate the effect of regional climate change associated with the effect of marine transgressions on the $\delta^{18}O_p$ pattern. Finally, comparison of simulations with varied elevation (Mio_278, Mio_450, Mio_278_plusAlps, Mio_450_plus_Alps, Mio_278_noAlps, and Mio_450_noAlps) contributes to our understanding of the potential $\delta^{18}O_p$ signal associated with topographic uplift. In the following, we organize our discussion around the implications of model-predicted changes in Middle Miocene $\delta^{18}O_p$, the different drivers behind these changes (global change vs. surface uplift) and their effect on interpretations of $\delta^{18}O$ records preserved in paleosol carbonates.

5.3.1. Changes in $\delta^{18}O_p$ Linked to Global Climate Forcing

Variations in temperature, humidity, precipitation, and wind directions are often considered as first-order variables contributing to the distribution pattern of $\delta^{18}O_p$ values (Dansgaard, 1953; Gat, 1996). The temperature increase in the Middle Miocene simulations shifts $\delta^{18}O_p$ values toward less negative values as a direct consequence of the Raleigh distillation process (Dansgaard, 1953; Gat, 1996). Both $\delta^{18}O_v$ and $\delta^{18}O_p$ reach their maximum in May–June, which coincides with the warm season. However, in the case of Middle Miocene Europe, the temperature effect is largely counterbalanced by changes in relative humidity. This is because $\delta^{18}O_v$ decreases with decreasing relative humidity during condensation through Rayleigh distillation. Our model results suggest that relative humidity decreases in Southern and central Europe during the Middle Miocene, which drives $\delta^{18}O_v$ toward more negative values. This mechanism is most efficient in August–September when relative humidity drops by ~20% (Figure 9c).

A decrease in relative humidity further contributes to changes in $\delta^{18}O_p$ by enhancing post-condensation effects, for example, raindrop evaporation. Since ^{16}O evaporates more easily, rain re-evaporation leads to an increase in $\delta^{18}O_p$ values of raindrops reaching the Earth surface. Therefore, the more re-evaporation occurs, the greater the difference between $\delta^{18}O_v$ and $\delta^{18}O_p$ values (see e.g., Lee & Fung, 2008). The pronounced difference between $\delta^{18}O_v$ and $\delta^{18}O_p$ from July to October in the Mio_278 and Mio_450 simulations is an indication of enhanced post-condensation effects occurring after initial condensation (Figures 9e and 9f).

Simulated Middle Miocene decrease in $\delta^{18}O_v$ in the late summer is most pronounced over the Balkans, which coincides with an area of enhanced atmospheric subsidence (Figure S10 in Supporting Information S1). The effect of subsidence in decreasing $\delta^{18}O_v$ has previously been shown by Frankenberg et al. (2009) and by Galewsky and Hurley (2010). Our results suggest (Figure 11) that the subsidence is located broadly over the Mediterranean, but drying and its isotopic effect occurs primarily over land. This is because over the ocean the boundary layer is efficiently separated from the free troposphere by an inversion, allowing it to be replenished by unlimited surface evaporation (Benetti et al., 2015). In contrast, over land, surface evaporation is limited, so that surface evaporation cannot compensate for the drying effect of subsidence.

5.3.2. Change in $\delta^{18}O_p$ Linked to the Regional Climate

In addition to the impact of global climate, $\delta^{18}O_p$ is influenced by regional changes of climate, land-sea cover, and topography. However, in our simulations, $\delta^{18}O_p$ values over the Alpine region are not sensitive to for example, the retreat of the Paratethys. The simulated changes between the control experiment and the experiment with modified land-sea distribution are below 1‰ (Figures 8e and 8f). These small changes could be explained by the fact that the Paratethys lies outside of major wind directions for Europe (Figure S10 in Supporting Information S1). However, this result is potentially linked to limitations of our modeling methodology, that is, the application of an atmospheric-only, not a fully coupled atmosphere-ocean GCM. Application of a GCM with a comprehensive simulation of marine circulation might result in higher SSTs over the Paratethys region and thus increase evaporation and contribution of this moisture source to the local hydroclimate in Europe.

Differences in $\delta^{18}O_p$ values between pairs of simulations with different topography within each pCO_2 setup are up to 8‰ (e.g., Figures 7c and 7f). The maximum changes are found between experiments with doubling of present Alpine elevation (Mio_278_plusAlps, Mio_450_plus_Alps) and an elevation that is reduced to 250 m (Mio_278_noAlps, Mio_450_noAlps). However, $\delta^{18}O_p$ changes between the experiments with varied topography are strongly limited to the area where the topography has been actually modified by the experimental setup. These findings for the Middle Miocene climate simulations are consistent with results of sensitivity experiments with pre-industrial boundary conditions but varied Alpine elevation (Botsyun et al., 2020). Given this limited-area impact, we hypothesize that $\delta^{18}O_p$ increase/decrease for experiments with higher/lower topography is mainly due to changes in local temperature and orographic precipitation.

5.4. Consequences for Paleoelevation Estimates

Our results for Middle Miocene seasonality changes in temperature and precipitation in Europe may have impacts for the interpretation of paleosol carbonate $\delta^{18}O$ or other isotope proxy data used for paleoelevation reconstructions of the Alps. When pedogenic carbonates are used to assess low-elevation $\delta^{18}O_p$ estimates, the MAT has typically been assumed for carbonate-water fractionation temperatures (e.g., Cerling et al., 1993; Garzione et al., 2000; Quade et al., 2011; Xu et al., 2013). This is based on the assumption that pedogenic carbonates form during conditions reflective of the mean growing season environment, which would typically imply soil temperature conditions between average and the maximum annual soil temperature (Cerling et al., 1993). However, changes in precipitation seasonality and the amplitude of seasonal temperature variation impacts the growth season of soil carbonates (Breecker et al., 2009; Burgener et al., 2016; Gallagher & Sheldon, 2016; Kelson et al., 2020; Peters et al., 2013). With the growing amount of paleosol carbonate formation temperature estimates based on clumped isotope (Δ_{47}) analyses, the timing of carbonate formation during the annual cycle becomes key (e.g., Gallagher et al., 2019; Kelson et al., 2020; Passey et al., 2010; Peters et al., 2013; Quade et al., 2013). Previous work has documented that carbonate in modern soils can precipitate at times of excessive dryness when climate conditions differ strongly from the mean growing season conditions (Breecker et al., 2009). However, carbonate precipitation may occur at different times of the year under different climate regimes and a complicated seasonal bias may strongly affect the formation and isotopic composition of pedogenic carbonate (e.g., Gallagher & Sheldon, 2016).

For the case of the European Alps in the Middle Miocene, prolonged warm seasons might bias carbonate $\delta^{18}O$ toward annual mean values, while stronger precipitation seasonality with very dry summers might bias carbonate $\delta^{18}O$ toward spring or autumn values. Our model-derived seasonal temperature shifts of >16°C (summer/JJA minus winter/DJF) predicted in the Mio_278 and Mio_450 simulations are similar to the observed Δ_{47}-based carbonate formation temperature change in the North Alpine Foreland Basin (Methner et al., 2020). These authors attributed this large shift in paleosol carbonate Δ_{47}-temperatures to at least partly reflect a shift in carbonate formation/preservation seasonality in conjunction with global cooling across the MMCT. They suggest a modification in rainfall seasonality across the MMCT and reorganization of mid-latitude atmospheric circulation across central Europe to account for hypothesized shift in carbonate formation/preservation seasonality.

Recently, Krsnik et al. (2021) used a combined pedogenic carbonate $\delta^{18}O$ value and Δ_{47} temperature (30°C ± 4°C) to reconstruct a near sea level $\delta^{18}O_p$ value of −5.6 ± 0.2‰ during the Middle Miocene (~14.5 Ma). In combination with a high-Alpine meteoric water δD record these results suggest that the central Alps attained surface elevations of >4,000 m no later than the mid-Miocene. The results of our new Middle Miocene experiments indicate that $\delta^{18}O$ varies on an annual scale between −4.9 and −7.6‰ (depending on the experimental setup) for the Northern Alps Foreland Basin. We suggest that only 1–2 ‰ of this variation is linked to changes in global climate. Thus, high elevation of the central Alps in the Middle Miocene is highly possible and supported by the results presented here. However, caution is needed regarding the timing of the carbonate formation and its potential bias on reconstructed $\delta^{18}O_p$ values. Moreover, our Middle Miocene experiments indicate a shallowing of the elevation-$\delta^{18}O_p$ gradient in the Middle Miocene Alps, permitting a possible underestimation of elevations derived from paleo-$\delta^{18}O_p$ data using present-day relationships.

6. Summary and Conclusions

We present high-resolution isotope-enabled ECHAM5-wiso experiments to study Middle Miocene climate and related $\delta^{18}O_p$ signals in Europe. Previous modeling efforts simulating the Middle Miocene climate have been recently joined in MioMIP1 and summarized in Burls et al. (2021). However, low resolution of MioMIP1 simulations (T31 or T42) do not provide a good representation of mountain topography in Europe, leading to: (a) an underestimation of surface temperature in mountain regions, and (b) an underestimation of precipitation. Moreover, it has been previously shown that the low resolution (e.g., T31), typical of past global coupled paleoclimate simulations, are unlikely to properly capture humidity behavior (Sherwood et al., 2010).

We have tackled this problem in generating much higher resolution (grid spacing of ~0.75°) simulations using the ECHAM5-wiso atmosphere GCM. Our new Middle Miocene simulations show 3.4°C–6.2°C higher temperatures in central Europe when compared to the pre-industrial, depending on the CO_2 setup. This result is in good agreement with temperatures derived using the proxy data, however, these results have a warm bias for low-elevation areas when compared to the Middle Miocene experiments participating in the MioMIP1 project. The simulated Middle Miocene precipitation is 300–500 mm/yr lower than in the pre-industrial times, which is consistent with estimates from herpetofaunal fossil proxy data. However, it is lower than predicted by paleobotanical (coexistence approach) proxy data. We attribute this precipitation change in Europe to shifts in large-scale pressure patterns in the North Atlantic and over Europe, namely an anticyclonic circulation centered over the Mediterranean and Southern Europe in winter, in addition to a deepened Icelandic Low in the summer. These ultimately result in a northward shift of the Atlantic storm track with a deflection of storms north of the Mediterranean into higher latitudes.

The simulated annual mean $\delta^{18}O_p$ pattern for the Middle Miocene is consistent with pre-industrial $\delta^{18}O_p$ across Europe in both its pattern and magnitude. The Middle Miocene global climate forcing has contributed to a maximum $\delta^{18}O_p$ increase of ~2‰ over the high Alpine elevation and to ~1‰ over low elevation. However, differences between PI and Middle Miocene simulations at seasonal scale are stronger (~3‰), especially when higher pCO_2 concentration is considered. The most striking difference is the $\delta^{18}O_p$ decrease in the late summer, driven by a drop of relative humidity, which coincides with enhanced atmospheric subsidence. Experiments with varied elevations of the Alps show that doubling of Alps elevation causes a maximum $\delta^{18}O_p$ decrease, up to 8‰ when compared to the experiment with non-changed topography. However, the isotope lapse rate in the central Alps shallows by 0.03‰/100 m for Middle Miocene setting.

We conclude that higher-resolution paleoclimate modeling is critical to capture regional paleoclimate variability. We suggest that Alpine paleoclimate and paleoaltimetry research would benefit from future studies focusing on (a) using proxies to constrain not only surface temperature and precipitation amount, but also relative humidity (e.g., using triple oxygen isotopic composition of phytoliths [Outrequin et al., 2021]) or the average chain length of n-alkanes (Eley & Hren, 2018), (b) studying the Miocene climate on orbital time scales, given the Miocene climate has been shown to be sensitive to the orbital forcing (Marzocchi et al., 2015) and the insolation changes have a potential impact on temperature in warmer climate (Samakinwa et al., 2020), (c) multi-model isotope enabled studies to avoid warm/cool bias in individual models, and (d) coupling of $\delta^{18}O$ proxy records and outputs of isotope-enabled GCM forced by constrained paleogeography (e.g., time appropriate land-sea distribution and different scenarios for orogens) and atmospheric pCO_2 for specific geological time periods investigated. This combination could help refine calibration of paleo $\delta^{18}O_p$-elevation relationships and refining paleoelevation estimates.

Conflict of Interest

The authors declare no conflicts of interest relevant to this study.

Data Availability Statement

The ECHAM model is available under the conditions of the "MPI-M Software Licence Agreement", which must be signed by each user. The "MPI-M Software Licence Agreement" and the information on the distribution of MPI-M models are given on: https://mpimet.mpg.de/fileadmin/projekte/ICON-ESM/mpi-m_sla_201202.pdf. The code of the isotopic version ECHAM5-wiso (Werner et al., 2011) is available upon request on the GitLab repository of the Alfred Wegener Institute (Germany): https://gitlab.awi.de/mwerner/mpi-esm-wiso (registration and a login is required). The ECHAM5-wiso modeling results are available in netcdf format at Botsyun et al. (2022).

Acknowledgments
This study was supported by the German Research Foundation (DFG) Grants EH329/19-1, 23-1 (to T.A.E.), MU4188/1-1, 3-1 (to S.G.M.), DFG ME 4955/1-1 (to K.M.), and DFG MU 2845/6-1 (to A.M.) as part of DFG Priority Program MB-4D (SPP-2017). K.M. further acknowledges support through a Feodor-Lynen-Fellowship by the Alexander-von-Humboldt foundation. A.K. is supported through Humboldt Research Fellowship for experienced researchers by the Alexander-von-Humboldt foundation. The authors thank R. Paul Acosta, Lin Li, and an anonymous reviewer for their constructive comments and recommendations, which highly improved this study. This work used computing resources of the Deutsches Klimarechenzentrum (DKRZ) granted by its Scientific Steering Committee (WLA) under project bb1200. Open Access funding enabled and organized by Projekt DEAL.

References

Abdul Aziz, H., Sanz-Rubio, E., Calvo, J. P., Hilgen, F. J., & Krijgsman, W. (2003). Paleoenvironmental reconstruction of a Middle Miocene alluvial fan to cyclic shallow lacustrine depositional system in the Calatayud Basin (NE Spain). *Sedimentology*, *50*(2), 211–236. https://doi.org/10.1046/j.1365-3091.2003.00544.x

Acosta, R. P., & Huber, M. (2017). The neglected Indo-Gangetic Plains low-level jet and its importance for moisture transport and precipitation during the peak summer monsoon. *Geophysical Research Letters*, *44*(16), 8601–8610. https://doi.org/10.1002/2017GL074440

Acosta, R. P., & Huber, M. (2020). Competing topographic mechanisms for the summer Indo-Asian monsoon. *Geophysical Research Letters*, *47*(3). https://doi.org/10.1029/2019GL085112

Benetti, M., Aloisi, G., Reverdin, G., Risi, C., & Sèze, G. (2015). Importance of boundary layer mixing for the isotopic composition of surface vapor over the subtropical North Atlantic Ocean. *Journal of Geophysical Research: Atmospheres*, *120*(6), 2190–2209. https://doi.org/10.1002/2014jd021947

Böhme, M., Bruch, A. A., & Selmeier, A. (2007). The reconstruction of Early and Middle Miocene climate and vegetation in Southern Germany as determined from the fossil wood flora. *Paleogeography, Paleoclimatology, Paleoecology*, *253*(1–2), 91–114.

Böhme, M., & Vasilyan, D. (2014). Ectothermic vertebrates from the late Middle Miocene of Gratkorn (Austria, Styria). *Paleobiodiversity and Paleoenvironments*, *94*(1), 21–40.

Böhme, M., Winklhofer, M., & Ilg, A. (2011). Miocene precipitation in Europe: Temporal trends and spatial gradients. *Paleogeography, Paleoclimatology, Paleoecology*, *304*(3–4), 212–218.

Boateng, D., Mutz, S. G., Ballian, A., Meijers, J. M. M., Methner, K., Botsyun, S., et al. (2022). The effects of diachronous surface uplift of the European Alps on regional climate and the oxygen isotopic composition of precipitation. *Climate of the Past Discusscussions*.

Botsyun, S., & Ehlers, T. A. (2021). How can climate models be used in paleoelevation reconstructions? *Frontiers of Earth Science*, *9*, 28. https://doi.org/10.3389/feart.2021.624542

Botsyun, S., Ehlers, T. A., Koptev, A., Böhme, M., Methner, K., Risi, C., et al. (2022). Middle Miocene climate and stable oxygen isotopes in Europe. [Dataset]. Zenodo. https://zenodo.org/record/6308475#.Y0gmDSFS-2w

Botsyun, S., Ehlers, T. A., Mutz, S. G., Methner, K., Krsnik, E., & Mulch, A. (2020). Opportunities and challenges for paleoaltimetry in "small" orogens: Insights from the European Alps. *Geophysical Research Letters*, *47*, e2019GL086046. https://doi.org/10.1029/2019GL086046

Botsyun, S., Sepulchre, P., Donnadieu, Y., Risi, C., Licht, A., & Caves Rugenstein, J. K. (2019). Revised paleoaltimetry data show low Tibetan Plateau elevation during the Eocene. *Science*, *363*(6430), eaaq1436. https://doi.org/10.1126/science.aaq1436

Botsyun, S., Sepulchre, P., Risi, C., & Donnadieu, Y. (2016). Impacts of Tibetan Plateau uplift on atmospheric dynamics and associated precipitation $\delta^{18}O$. *Climate of the Past*, *12*(6), 1401–1420. https://doi.org/10.5194/cp-12-1401-2016

Bouchal, J. M., Güner, T. H., & Denk, T. (2018). Middle Miocene climate of southwestern Anatolia from multiple botanical proxies. *Climate of the Past*, *14*(10), 1427–1440. https://doi.org/10.5194/cp-14-1427-2018

Breecker, D. O., Sharp, Z. D., & McFadden, L. D. (2009). Seasonal bias in the formation and stable isotopic composition of pedogenic carbonate in modern soils from central New Mexico, USA. *Bulletin of the Geological Society of America*, *121*(3–4), 630–640. https://doi.org/10.1130/B26413.1

Brovkin, V., Raddatz, T., Reick, C. H., Claussen, M., & Gayler, V. (2009). Global biogeophysical interactions between forest and climate. *Geophysical Research Letters*, *36*(7). https://doi.org/10.1029/2009gl037543

Bruch, A. A., Uhl, D., & Mosbrugger, V. (2007). Miocene climate in Europe—patterns and evolution: A first synthesis of NECLIME.

Bruch, A. A., Utescher, T., & Mosbrugger, V. (2011). Precipitation patterns in the Miocene of central Europe and the development of continentality. *Paleogeography, Paleoclimatology, Paleoecology*, *304*(3), 202–211. https://doi.org/10.1016/j.palaeo.2010.10.002

Burgener, L., Huntington, K. W., Hoke, G. D., Schauer, A., Ringham, M. C., Latorre, C., & Díaz, F. P. (2016). Variations in soil carbonate formation and seasonal bias over> 4 km of relief in the western Andes (30°S) revealed by clumped isotope thermometry. *Earth and Planetary Science Letters*, *441*, 188–199. https://doi.org/10.1016/j.epsl.2016.02.033

Burls, N. J., Bradshaw, C. D., De Boer, A. M., Herold, N., Huber, M., Pound, M., et al. (2021). Simulating Miocene warmth: Insights from an opportunistic Multi-Model ensemble (MioMIP1). *Paleoceanography and Paleoclimatology*, *36*, e2020PA004054. https://doi.org/10.1029/2020PA004054

Campani, M., Mulch, A., Kempf, O., Schlunegger, F., & Mancktelow, N. (2012). Miocene paleotopography of the central Alps. *Earth and Planetary Science Letters*, *337–338*, 174–185. https://doi.org/10.1016/j.epsl.2012.05.017

Caves, J. K., Winnick, M. J., Graham, S. A., Sjostrom, D. J., Mulch, A., & Chamberlain, C. P. (2015). Role of the westerlies in central Asia climate over the Cenozoic. *Earth and Planetary Science Letters*, *428*, 33–43. https://doi.org/10.1016/j.epsl.2015.07.023

Cerling, T. E., Wang, Y., & Quade, J. (1993). Expansion of C4 ecosystems as an indicator of global ecological change in the late Miocene. *Nature*, *361*(6410), 344–345. https://doi.org/10.1038/361344a0

Chandler, M. A., Rind, D., & Ruedy, R. (1992). Pangean climate during the Early Jurassic: GCM simulations and the sedimentary record of paleoclimate. *The Geological Society of America Bulletin*, *104*(5), 543–559. https://doi.org/10.1130/0016-7606(1992)104<0543:pcdtej>2.3.co;2

Cui, Y., Schubert, B. A., & Jahren, A. H. (2020). A 23 m.y. record of low atmospheric CO_2. *Geology*, *48*(9), 888–892. https://doi.org/10.1130/g47681.1

Dansgaard, W. (1953). The abundance of O^{18} in atmospheric water and water vapor. *Tellus*, *5*(4), 461–469. https://doi.org/10.3402/tellusa.v5i4.8697

Dee, D. P., Uppala, S. M., Simmons, A. J., Berrisford, P., Poli, P., Kobayashi, S., et al. (2011). The ERA-Interim reanalysis: Configuration and performance of the data assimilation system. *Quarterly Journal of the Royal Meteorological Society*, *137*(656), 553–597. https://doi.org/10.1002/qj.828

Dietrich, S., Werner, M., Spangehl, T., & Lohmann, G. (2013). Influence of orbital forcing and solar activity on water isotopes in precipitation during the mid- and late Holocene. *Climate of the Past*, *9*(1), 13–26. https://doi.org/10.5194/cp-9-13-2013

Ehlers, T. A., & Poulsen, C. J. (2009). Influence of Andean uplift on climate and paleoaltimetry estimates. *Earth and Planetary Science Letters*, *281*(3–4), 238–248. https://doi.org/10.1016/j.epsl.2009.02.026

Eizenhöfer, P. R., Glotzbach, C., Büttner, L., Kley, J., & Ehlers, T. A. (2021). Turning the orogenic switch: Slab-reversal in the Eastern Alps recorded by low-temperature thermochronology. *Geophysical Research Letters*, *48*(6), e2020GL092121. https://doi.org/10.1029/2020GL092121

Eley, Y. L., & Hren, M. T. (2018). Reconstructing vapor pressure deficit from leaf wax lipid molecular distributions. *Scientific Reports*, *8*(1), 1–8. https://doi.org/10.1038/s41598-018-21959-w

Eronen, J. T., Fortelius, M., Micheels, A., Portmann, F. T., Puolamäki, K., & Janis, C. M. (2012). Neogene aridification of the Northern Hemisphere. *Geology*, *40*(9), 823–826. https://doi.org/10.1130/g33147.1

Feakins, S. J., Warny, S., & Lee, J. E. (2012). Hydrologic cycling over Antarctica during the Middle Miocene warming. *Nature Geoscience*, *5*(8), 557–560. https://doi.org/10.1038/ngeo1498

Foster, G. L., & Rohling, E. J. (2013). Relationship between sea level and climate forcing by CO_2 on geological timescales. *Proceedings of the National Academy of Sciences of the United States of America*, *110*(4), 1209–1214. https://doi.org/10.1073/pnas.1216073110

Frankenberg, C., Yoshimura, K., Warneke, T., Aben, I., Butz, A., Deutscher, N., et al. (2009). Dynamic processes governing lower-tropospheric HDO/H_2O ratios as observed from space and ground. *Science*, *325*(5946), 1374–1377. https://doi.org/10.1126/science.1173791

Gaetani, M., Pohl, B., Douville, H., & Fontaine, B. (2011). West African monsoon influence on the summer Euro-Atlantic circulation. *Geophysical Research Letters*, *38*(9). https://doi.org/10.1029/2011gl047150

Galewsky, J., & Hurley, J. V. (2010). An advection-condensation model for subtropical water vapor isotopic ratios. *Journal of Geophysical Research*, *115*(D16). https://doi.org/10.1029/2009jd013651

Gallagher, T. M., Hren, M., & Sheldon, N. D. (2019). The effect of soil temperature seasonality on climate reconstructions from paleosols. *American Journal of Science*, *319*(7), 549–581. https://doi.org/10.2475/07.2019.02

Gallagher, T. M., & Sheldon, N. D. (2016). Combining soil water balance and clumped isotopes to understand the nature and timing of pedogenic carbonate formation. *Chemical Geology*, *435*, 79–91. https://doi.org/10.1016/j.chemgeo.2016.04.023

Garzione, C. N., Dettman, D. L., Quade, J., De Celles, P. G., & Butler, R. F. (2000). High times on the Tibetan Plateau: Paleoelevation of the Thakkhola graben, Nepal. *Geology*, *28*(4), 339–342. https://doi.org/10.1130/0091-7613(2000)028<0339:htottp>2.3.co;2

Gaskell, D. E., Huber, M., O'Brien, C. L., Inglis, G. N., Acosta, R. P., Poulsen, C. J., & Hull, P. M. (2022). The latitudinal temperature gradient and its climate dependence as inferred from foraminiferal $\delta^{18}O$ over the past 95 Myr. *Proceedings of the National Academy of Sciences of the United States of America*, *119*(11), 1–8. https://doi.org/10.1073/pnas.2111332119

Gat, J. R. (1996). Oxygen and hydrogen isotopes in the hydrologic cycle. *Annual Review of Earth and Planetary Sciences*, *24*(1), 225–262. https://doi.org/10.1146/annurev.earth.24.1.225

Giorgi, F., & Lionello, P. (2008). Climate change projections for the Mediterranean region. *Global and Planetary Change*, *63*(2–3), 90–104. https://doi.org/10.1016/j.gloplacha.2007.09.005

Greenop, R., Foster, G. L., Wilson, P. A., & Lear, C. H. (2014). Middle Miocene climate instability associated with high-amplitude CO_2 variability. *Paleoceanography*, *29*(9), 845–853. https://doi.org/10.1002/2014pa002653

Grimm, G. W., & Denk, T. (2012). Reliability and resolution of the coexistence approach—a revalidation using modern-day data. *Review of Palaeobotany and Palynology*, *172*, 33-47.

Hagemann, S. (2002). An improved land surface parameter data set for global and regional climate models. In *Max Planck Institute for Meteorology Report* (Vol. 162). MPI for Meteorology.

Handy, M. R., Schmid, S. M., Bousquet, R., Kissling, E., & Bernoulli, D. (2010). Reconciling plate-tectonic reconstructions of Alpine Tethys with the geological-geophysical record of spreading and subduction in the Alps. *Earth-Science Reviews*, *102*(3–4), 121–158. https://doi.org/10.1016/j.earscirev.2010.06.002

Hergarten, S., Wagner, T., & Stüwe, K. (2010). Age and prematurity of the Alps derived from topography. *Earth and Planetary Science Letters*, *297*(3–4), 453–460. https://doi.org/10.1016/j.epsl.2010.06.048

Herold, N., Huber, M., & Müller, R. D. (2011). Modeling the Miocene climatic optimum. Part I: Land and atmosphere. *Journal of Climate*, *24*(24), 6353–6372. https://doi.org/10.1175/2011jcli4035.1

Herold, N., Seton, M., Müller, R. D., You, Y., & Huber, M. (2008). Middle Miocene tectonic boundary conditions for use in climate models. *Geochemistry, Geophysics, Geosystems*, *9*(10). https://doi.org/10.1029/2008GC002046

Huang, X., Stärz, M., Gohl, K., Knorr, G., & Lohmann, G. (2017). Impact of Weddell Sea shelf progradation on Antarctic bottom water formation during the Miocene. *Paleoceanography*, *32*(3), 304–317. https://doi.org/10.1002/2016PA002987

Ingram, W., & Bushell, A. C. (2021). Sensitivity of climate feedbacks to vertical resolution in a general circulation model. *Geophysical Research Letters*, *48*(12), 1–9. https://doi.org/10.1029/2020GL092268

Insel, N., Poulsen, C. J., Ehlers, T. A., & Sturm, C. (2012). Response of meteoric $\delta^{18}O$ to surface uplift–Implications for Cenozoic Andean Plateau growth. *Earth and Planetary Science Letters*, *317–318*, 262–272. https://doi.org/10.1016/j.epsl.2011.11.039

IPCC. (2013). Climate change 2013: The physical science basis. In T. F. Stocker, D. Qin, G.-K. Plattner, M. Tignor, S. K. Allen, J. Boschung, et al. (Eds.), *Contribution of Working Group I to the Fifth Assessment Report of the Intergovernmental Panel on Climate Change*. Cambridge University Press.

Jäger, E., & Hantke, R. (1984). Evidenzen für die Vergletscherung eines Alpinen Bergeller Hochgebirges an der Grenze Oligozän/Miozän. *Geologische Rundschau*, *73*(2), 567–575.

Kelson, J. R., Huntington, K. W., Breecker, D. O., Burgener, L. K., Gallagher, T. M., Hoke, G. D., & Petersen, S. V. (2020). A proxy for all seasons? A synthesis of clumped isotope data from Holocene soil carbonates. *Quaternary Science Reviews*, *234*, 106259. https://doi.org/10.1016/j.quascirev.2020.106259

Knorr, G., Butzin, M., Micheels, A., & Lohmann, G. (2011). A warm Miocene climate at low atmospheric CO_2 levels. *Geophysical Research Letters*, *38*(20). https://doi.org/10.1029/2011GL048873

Knutti, R., & Sedláček, J. (2013). Robustness and uncertainties in the new CMIP5 climate model projections. *Nature Climate Change*, *3*(4), 369–373. https://doi.org/10.1038/nclimate1716

Kocsis, L., Vennemann, T. W., & Fontignie, D. (2007). Migration of sharks into freshwater systems during the Miocene and implications for Alpine paleoelevation. *Geology*, *35*(5), 451–454. https://doi.org/10.1130/g23404a.1

Krsnik, E., Methner, K., Campani, M., Botsyun, S., Mutz, S. G., Ehlers, T. A., et al. (2021). Miocene high elevation in the Central Alps. *Solid Earth*, *12*(11), 2615-2631. https://doi.org/10.5194/se-12-2615-2021

Kuhlemann, J. (2007). Paleogeographic and paleotopographic evolution of the Swiss and eastern Alps since the Oligocene. *Global and Planetary Change*, *58*(1–4), 224–236. https://doi.org/10.1016/j.gloplacha.2007.03.007

Kukla, T., Winnick, M. J., Maher, K., Ibarra, D. E., & Chamberlain, C. P. (2019). The sensitivity of terrestrial $\delta^{18}O$ gradients to hydroclimate evolution. *Journal of Geophysical Research: Atmospheres*, *124*(2), 563–582. https://doi.org/10.1029/2018jd029571

Langebroek, P. M., Paul, A., & Schulz, M. (2009). Antarctic ice-sheet response to atmospheric CO_2 and insolation in the Middle Miocene. *Climate of the Past*, *5*(4), 633–646. https://doi.org/10.5194/cp-5-633-2009

Langebroek, P. M., Paul, A., & Schulz, M. (2010). Simulating the sea level imprint on marine oxygen isotope records during the Middle Miocene using an ice sheet-climate model. *Paleoceanography*, *25*(4). https://doi.org/10.1029/2008pa001704

Langebroek, P. M., Werner, M., & Lohmann, G. (2011). Climate information imprinted in oxygen-isotopic composition of precipitation in Europe. *Earth and Planetary Science Letters*, *311*(1–2), 144–154. https://doi.org/10.1016/j.epsl.2011.08.049

Lee, J. E., & Fung, I. (2008). "Amount effect" of water isotopes and quantitative analysis of post-condensation processes. *Hydrological Processes*, *22*(1), 1–8. https://doi.org/10.1002/hyp.6637

Lelieveld, J., Berresheim, H., Borrmann, S., Crutzen, P. J., Dentener, F. J., Fischer, H., et al. (2002). Global air pollution crossroads over the Mediterranean. *Science*, *298*(5594), 794–799. https://doi.org/10.1126/science.1075457

Licht, A., van Cappelle, M., Abels, H. A., Ladant, J.-B., Trabucho-Alexandre, J., France-Lanord, C., et al. (2014). Asian monsoons in a late Eocene greenhouse world. *Nature*, *513*(7519), 501–506. https://doi.org/10.1038/nature13704

Lorenz, S. J., & Lohmann, G. (2004). Acceleration technique for Milankovitch type forcing in a coupled atmosphere-ocean circulation model: Method and application for the Holocene. *Climate Dynamics*, *23*(7–8), 727–743. https://doi.org/10.1007/s00382-004-0469-y

Lott, F. (1999). Alleviation of stationary biases in a GCM through a mountain drag parameterization scheme and a simple representation of mountain lift forces. *Monthly Weather Review*, *127*(5), 788–801. https://doi.org/10.1175/1520-0493(1999)127<0788:aosbia>2.0.co;2

Lott, F., & Miller, M. J. (1997). A new subgrid-scale orographic drag parametrization: Its formulation and testing. *Quarterly Journal of the Royal Meteorological Society*, *123*(537), 101–127. https://doi.org/10.1002/qj.49712353704

Marzocchi, A., Lunt, D. J., Flecker, R., Bradshaw, C. D., Farnsworth, A., & Hilgen, F. J. (2015). Orbital control on late Miocene climate and the North African monsoon: Insight from an ensemble of sub-precessional simulations. *Climate of the Past*, *11*(10), 1271–1295. https://doi.org/10.5194/cp-11-1271-2015

Methner, K., Campani, M., Fiebig, J., Löffler, N., Kempf, O., & Mulch, A. (2020). Middle Miocene long-term continental temperature change in and out of pace with marine climate records. *Scientific Reports*, *10*(1), 1–10. https://doi.org/10.1038/s41598-020-64743-5

Mosbrugger, V., & Utescher, T. (1997). The coexistence approach—A method for quantitative reconstructions of tertiary terrestrial paleoclimate data using plant fossils. *Paleogeography, Paleoclimatology, Paleoecology*, *134*(1–4), 61–86. https://doi.org/10.1016/s0031-0182(96)00154-x

Mulch, A. (2016). Stable isotope paleoaltimetry and the evolution of landscapes and life. *Earth and Planetary Science Letters*, *433*, 180–191. https://doi.org/10.1016/j.epsl.2015.10.034

Muñoz-Sabater, J., Dutra, E., Agustí-Panareda, A., Albergel, C., Arduini, G., Balsamo, G., et al. (2021). ERA5-Land: A state-of-the-art global reanalysis data set for land applications. *Earth System Science Data*, *13*(9), 4349–4383.

Mutz, S. G., Ehlers, T. A., Werner, M., Lohmann, G., Stepanek, C., & Li, J. (2018). Estimates of late Cenozoic climate change relevant to Earth surface processes in tectonically active orogens. *Earth Surface Dynamics*, *6*(2), 271–301. https://doi.org/10.5194/esurf-6-271-2018

Outrequin, C., Alexandre, A., Vallet-Coulomb, C., Piel, C., Devidal, S., Landais, A., et al. (2021). The triple oxygen isotope composition of phytoliths, a new proxy of atmospheric relative humidity: Controls of soil water isotope composition, temperature, CO_2 concentration, and relative humidity. *Climate of the Past*, *17*(5), 1881–1902. https://doi.org/10.5194/cp-17-1881-2021

Pagani, M., Arthur, M. A., & Freeman, K. H. (1999). Miocene evolution of atmospheric carbon dioxide. *Paleoceanography*, *14*(3), 273–292. https://doi.org/10.1029/1999pa900006

Passey, B. H., Levin, N. E., Cerling, T. E., Brown, F. H., & Eiler, J. M. (2010). High-temperature environments of human evolution in East Africa based on bond ordering in paleosol carbonates. *Proceedings of the National Academy of Sciences of the United States of America*, *107*(25), 11245–11249. https://doi.org/10.1073/pnas.1001824107

Paul, A., Mulitza, S., Pätzold, J., & Wolff, T. (1999). Simulation of oxygen isotopes in a global ocean model. In *Use of proxies in paleoceanography* (pp. 655–686). Springer. https://doi.org/10.1007/978-3-642-58646-0_27

Peters, N. A., Huntington, K. W., & Hoke, G. D. (2013). Hot or not? Impact of seasonally variable soil carbonate formation on paleotemperature and O-isotope records from clumped isotope thermometry. *Earth and Planetary Science Letters*, *361*, 208–218. https://doi.org/10.1016/j.epsl.2012.10.024

Poage, M. A., & Chamberlain, C. P. (2001). Empirical relationships between elevation and the stable isotope composition of precipitation and surface waters: Considerations for studies of paleoelevation change. *American Journal of Science*, *301*(1), 1–15. https://doi.org/10.2475/ajs.301.1.1

Popov, S. V., Rögl, F., Rozanov, A. Y., Steininger, F. F., Shcherba, I. G., & Kovac, M. (2004). Lithological-paleogeographic maps of Paratethys-10 maps late Eocene to pliocene.

Poulsen, C. J., Ehlers, T. A., & Insel, N. (2010). Onset of convective rainfall during gradual late Miocene rise of the central Andes. *Science*, *328*(5977), 490–493. https://doi.org/10.1126/science.1185078

Quade, J., Breecker, D. O., Daëron, M., & Eiler, J. (2011). The paleoaltimetry of Tibet: An isotopic perspective. *American Journal of Science*, *311*(2), 77–115. https://doi.org/10.2475/02.2011.01

Quade, J., Eiler, J., Daeron, M., & Achyuthan, H. (2013). The clumped isotope geothermometer in soil and paleosol carbonate. *Geochimica et Cosmochimica Acta*, *105*, 92–107. https://doi.org/10.1016/j.gca.2012.11.031

Quade, J., Garzione, C., & Eiler, J. (2007). Paleoelevation reconstruction using pedogenic carbonates. *Reviews in Mineralogy and Geochemistry*, *66*(1), 53–87. https://doi.org/10.2138/rmg.2007.66.3

Quan, C., Liu, Y.-S. C., Tang, H., & Utescher, T. (2014). Miocene shift of European atmospheric circulation from trade wind to westerlies. *Scientific Reports*, *4*. https://doi.org/10.1038/srep05660

Raddatz, T. J., Reick, C. H., Knorr, W., Kattge, J., Roeckner, E., Schnur, R., et al. (2007). Will the tropical land biosphere dominate the climate-carbon cycle feedback during the twenty-first century? *Climate Dynamics*, *29*(6), 565–574. https://doi.org/10.1007/s00382-007-0247-8

Rae, J. W. B., Zhang, Y. G., Liu, X., Foster, G. L., Stoll, H. M., & Whiteford, R. D. M. (2021). Atmospheric CO_2 over the past 66 Myr from marine archives. *Annual Review of Earth and Planetary Sciences*, *49*. https://doi.org/10.1146/annurev-earth-082420-063026

Raymo, M. E., & Ruddiman, W. F. (1992). Tectonic forcing of late Cenozoic climate. *Nature*, *359*(6391), 117–122. https://doi.org/10.1038/359117a0

Rodwell, M. J., & Hoskins, B. J. (2001). Subtropical anticyclones and summer monsoons. *Journal of Climate*, *14*(15), 3192–3211. https://doi.org/10.1175/1520-0442(2001)014<3192:saasm>2.0.co;2

Roeckner, E., Bäuml, G., Bonaventura, L., Brokopf, R., Esch, M., Giorgetta, M., et al. (2003). *The atmospheric general circulation model ECHAM 5. PART I: Model description, Report No. 349*. Max-Planck-Institut für Meteorologie. Retrieved from http://hdl.handle.net/11858/00-001M-0000-0012-0144-5

Rowley, D. B., Pierrehumbert, R. T., & Currie, B. S. (2001). A new approach to stable isotope-based paleoaltimetry: Implications for paleoaltimetry and paleohypsometry of the High Himalaya since the late Miocene. *Earth and Planetary Science Letters*, *188*(1–2), 253–268. https://doi.org/10.1016/S0012-821X(01)00324-7

Ruddiman, W. F., & Kutzbach, J. E. (1989). Forcing of late Cenozoic Northern Hemisphere climate by plateau uplift in southern Asia and the American West. *Journal of Geophysical Research*, *94*(D15), 18409–18427. https://doi.org/10.1029/jd094id15p18409

Saaroni, H., & Ziv, B. (2000). Summer rain episodes in a Mediterranean climate, the case of Israel: Climatological-dynamical analysis. *International Journal of Climatology*, *20*(2), 191–209. https://doi.org/10.1002/(sici)1097-0088(200002)20:2<191::aid-joc464>3.0.co;2-e

Samakinwa, E., Stepanek, C., & Lohmann, G. (2020). Sensitivity of mid-Pliocene climate to changes in orbital forcing and PlioMIP's boundary conditions. *Climate of the Past*, *16*(4), 1643–1665. https://doi.org/10.5194/cp-16-1643-2020

Schlunegger, F., & Kissling, E. (2015). Slab rollback orogeny in the Alps and evolution of the Swiss Molasse basin. *Nature Communications*, *6*. https://doi.org/10.1038/ncomms9605

Schlunegger, F., Rieke-Zapp, D., & Ramseyer, K. (2007). Possible environmental effects on the evolution of the Alps-Molasse Basin system. *Swiss Journal of Geosciences*, *100*(3), 383–405. https://doi.org/10.1007/s00015-007-1238-9

Schmid, S. M., Pfiffner, O.-A., Froitzheim, N., Schönborn, G., & Kissling, E. (1996). Geophysical-geological transect and tectonic evolution of the Swiss-Italian Alps. *Tectonics*, *15*(5), 1036–1064. https://doi.org/10.1029/96tc00433

Sharp, Z. D. (2005). Stable isotope geochemistry and formation mechanisms of quartz veins; extreme paleoaltitudes of the central Alps in the Neogene. *American Journal of Science*, *305*(3), 187–219. https://doi.org/10.2475/ajs.305.3.187

Sherwood, S. C., Ingram, W., Tsushima, Y., Satoh, M., Roberts, M., Vidale, P. L., & O'Gorman, P. A. (2010). Relative humidity changes in a warmer climate. *Journal of Geophysical Research*, *115*(D9). https://doi.org/10.1029/2009jd012585

Shevenell, A. E., Kennett, J. P., & Lea, D. W. (2008). Middle Miocene ice sheet dynamics, deep-sea temperatures, and carbon cycling: A southern ocean perspective. *Geochemistry, Geophysics, Geosystems*, *9*(2). https://doi.org/10.1029/2007gc001736

Shields, C. A., Kiehl, J. T., Rush, W., Rothstein, M., & Snyder, M. A. (2021). Atmospheric rivers in high-resolution simulations of the Paleocene Eocene Thermal Maximum (PETM). *Paleogeography, Paleoclimatology, Paleoecology*, *567*, 110293. https://doi.org/10.1016/j.palaeo.2021.110293

Sosdian, S. M., Greenop, R., Hain, M. P., Foster, G. L., Pearson, P. N., & Lear, C. H. (2018). Constraining the evolution of Neogene ocean carbonate chemistry using the boron isotope pH proxy. *Earth and Planetary Science Letters*, *498*, 362–376. https://doi.org/10.1016/j.epsl.2018.06.017

Stampfli, G. M., Mosar, J., Marquer, D., Marchant, R., Baudin, T., & Borel, G. (1998). Subduction and obduction processes in the Swiss Alps. *Tectonophysics*, *296*(1–2), 159–204. https://doi.org/10.1016/s0040-1951(98)00142-5

Stärz, M., Jokat, W., Knorr, G., & Lohmann, G. (2017). Threshold in North Atlantic-Arctic Ocean circulation controlled by the subsidence of the Greenland-Scotland Ridge. *Nature Communications*, *8*, 15681.

Steinthorsdottir, M., Coxall, H. K., De Boer, A. M., Huber, M., Barbolini, N., Bradshaw, C. D., et al. (2021). The Miocene: The future of the past. *Paleoceanography and Paleoclimatology*, *36*(4), e2020PA004037. https://doi.org/10.1029/2020pa004037

Stepanek, C., & Lohmann, G. (2012). Modeling mid-Pliocene climate with COSMOS. *Geoscientific Model Development*, *5*, 1221–1243. https://doi.org/10.5194/gmd-5-1221-2012

Super, J. R., Thomas, E., Pagani, M., Huber, M., O'Brien, C., & Hull, P. M. (2018). North Atlantic temperature and pCO_2 coupling in the early-Middle Miocene. *Geology*, *46*(6), 519–522. https://doi.org/10.1130/g40228.1

Super, J. R., Thomas, E., Pagani, M., Huber, M., O'Brien, C. L., & Hull, P. M. (2020). Miocene evolution of North Atlantic sea surface temperature. *Paleoceanography and Paleoclimatology*, *35*(5), e2019PA003748. https://doi.org/10.1029/2019pa003748

Tyrlis, E., Lelieveld, J., & Steil, B. (2013). The summer circulation over the eastern Mediterranean and the Middle East: Influence of the South Asian monsoon. *Climate Dynamics*, *40*(5–6), 1103–1123. https://doi.org/10.1007/s00382-012-1528-4

Utescher, T., Bruch, A. A., Erdei, B., François, L., Ivanov, D., Jacques, F. M. B., et al. (2014). The coexistence approach—Theoretical background and practical considerations of using plant fossils for climate quantification. *Paleogeography, Paleoclimatology, Paleoecology*, *410*, 58–73. https://doi.org/10.1016/j.palaeo.2014.05.031

Valla, P. G., Sternai, P., & Fox, M. (2021). How climate, uplift and erosion shaped the Alpine topography. *Elements*, *17*(1), 41–46. https://doi.org/10.2138/gselements.17.1.41

Werner, M., Langebroek, P. M., Carlsen, T., Herold, M., & Lohmann, G. (2011). Stable water isotopes in the ECHAM5 general circulation model: Toward high-resolution isotope modeling on a global scale. *Journal of Geophysical Research*, *116*(15), 1–14. https://doi.org/10.1029/2011JD015681

Westerhold, T., Bickert, T., & Röhl, U. (2005). Middle to late Miocene oxygen isotope stratigraphy of ODP site 1085 (SE Atlantic): New constrains on Miocene climate variability and sea-level fluctuations. *Paleogeography, Paleoclimatology, Paleoecology*, *217*(3–4), 205–222. https://doi.org/10.1016/j.palaeo.2004.12.001

Worobiec, E., Widera, M., Worobiec, G., & Kurdziel, B. (2021). Middle Miocene palynoflora from the Adamów lignite deposit, central Poland. *Palynology*, *45*(1), 59–71. https://doi.org/10.1080/01916122.2019.1697388

Wright, J. D., Miller, K. G., & Fairbanks, R. G. (1992). Early and middle Miocene stable isotopes: Implications for deepwater circulation and climate. *Paleoceanography*, *7*(3), 357–389. https://doi.org/10.1029/92pa00760

Xu, Q., Ding, L., Zhang, L., Cai, F., Lai, Q., Yang, D., & Liu-Zeng, J. (2013). Paleogene high elevations in the Qiangtang Terrane, central Tibetan Plateau. *Earth and Planetary Science Letters*, *362*, 31–42. https://doi.org/10.1016/j.epsl.2012.11.058

Zamanian, K., Pustovoytov, K., & Kuzyakov, Y. (2016). Pedogenic carbonates: Forms and formation processes. *Earth-Science Reviews*, *157*, 1–17. https://doi.org/10.1016/j.earscirev.2016.03.003

Ziv, B., Saaroni, H., & Alpert, P. (2004). The factors governing the summer regime of the eastern Mediterranean. *International Journal of Climatology*, *24*(14), 1859–1871. https://doi.org/10.1002/joc.1113

References From the Supporting Information

Akgün, F., Kayseri, M. S., & Akkiraz, M. S. (2007). Palaeoclimatic evolution and vegetational changes during the Late Oligocene–Miocene period in Western and Central Anatolia (Turkey). *Palaeogeography, Palaeoclimatology, Palaeoecology*, *253*(1-2), 56–90.

Barrón, E., Rivas-Carballo, R., Postigo-Mijarra, J. M., Alcalde-Olivares, C., Vieira, M., Castro, L., et al. (2010). The Cenozoic vegetation of the Iberian Peninsula: a synthesis. *Review of palaeobotany and palynology*, *162*(3), 382–402.

Bruch, A. A., Utescher, T., Olivares, C. A., Doláková, N., Ivanov, D., & Mosbrugger, V. (2004). Middle and Late Miocene spatial temperature patterns and gradients in Europe-preliminary results based on palaeobotanical climate reconstructions. *Courier-Forschungsinstitut Senckenberg*, 15–28.

Chirilă, G., & Tabără, D. (2008). Palaeofloristic study of the Volhyian from Rasca (Moldavian Platform) - palaeoclimatic and palaeoenvironmental implications. *Acta Palaeontologica Romaniae*, *6*, 29–42.

Dahinden, F., Aemisegger, F., Wernli, H., Schneider, M., Diekmann, C. J., Ertl, B., et al. (2021). Disentangling different moisture transport pathways over the eastern subtropical North Atlantic using multi-platform isotope observations and high-resolution numerical modeling. *Atmospheric Chemistry and Physics*, *21*(21), 16319–16347. https://doi.org/10.5194/acp-21-16319-2021

Diekmann, C. J., Schneider, M., Knippertz, P., de Vries, A. J., Pfahl, S., Aemisegger, F., et al. (2021). A Lagrangian perspective on stable water isotopes during the West African monsoon. *Journal of Geophysical Research: Atmospheres*, *126*(19), 1–23. https://doi.org/10.1029/2021JD034895

Dütsch, M., Pfahl, S., Meyer, M., & Wernli, H. (2018). Lagrangian process attribution of isotopic variations in near-surface water vapor in a 30 yr regional climate simulation over Europe. *Atmospheric Chemistry and Physics*, *18*(3), 1653–1669. https://doi.org/10.5194/acp-18-1653-2018

Erdei, B., Hably, L., Kázmér, M., Utescher, T., & Bruch, A. A. (2007). Neogene flora and vegetation development of the Pannonian domain in relation to palaeoclimate and palaeogeography. *Palaeogeography, Palaeoclimatology, Palaeoecology*, *253*(1-2), 115–140.

Figueiral, I., Mosbrugger, V., Rowe, N. P., Utescher, T., Jones, T. P., & Von Der Hocht, F. (2002). Role of charcoal analysis for interpreting vegetation change and paleoclimate in the Miocene Rhine Embayment (Germany). *Palaios*, *17*(4), 347–365.

Goldner, A., Herold, N., & Huber, M. (2014). The challenge of simulating the warmth of the mid-Miocene climatic optimum in CESM1. *Climate of the Past*, *10*(2), 523–536. https://doi.org/10.5194/cp-10-523-2014

Ivanov, D. A., Ashraf, A. R., & Mosbrugger, V. (2007). Late Oligocene and Miocene climate and vegetation in the Eastern Paratethys area (northeast Bulgaria), based on pollen data. *Palaeogeography, Palaeoclimatology, Palaeoecology*, *255*(3-4), 342–360.

Kováčová, M., Hohenegger, J., & Ćorić, S. (2009). Palaeovegetation and climate based on pollen analysis of the Baden-Sooss section (Middle Miocene, Vienna Basin, Austria). In: Filipescu, S. (Ed.), *3rd International Workshop Neogene of Central and South-Eastern Europe*. Cluj University Press, (pp. 65-65). Cluj-Napoca.

Merlivat, L., & Jouzel, J. (1979). Global climatic interpretation of the deuterium-oxygen 18 relationship for precipitation. *Journal of Geophysical Research: Oceans*, *84*(C8), 5029–5033. https://doi.org/10.1029/jc084ic08p05029

Mosbrugger, V., Utescher, T., & Dilcher, D. L. (2005). Cenozoic continental climatic evolution of Central Europe. *Proceedings of the National Academy of Sciences*, *102*(42), 14964–14969. https://doi.org/10.1073/pnas.0505267102

Özer, K. M. S., & Akgün, F. (2010). The Late Burdigalian-Langhian interval in Turkey and the palaeoenvironmental and palaeoclimatic implications and correlation of Europe and Turkey: Late Burdigalian-Langhian palynofloras and palaeoclimatic properties of the Muğla-Milas (Kultak). *Geological Bulletin of Turkey*, *53*, 1–44.

Özer, M. S. K., Sozbilir, H., & Akgün, F. (2014). Miocene palynoflora of the Kocaçay and Cumaovası basins: a contribution to the synthesis of Miocene palynology, palaeoclimate, and palaeovegetation in western Turkey. *Turkish Journal of Earth Sciences*, *23*(3), 233–259.

Pais, J. (1981). Contribuição para o conhecimento da vegetação Miocénica da parte ocidental da Bacia do Tejo, [Ph.D. thesis], Universidade Nova de Lisboa, Portugal.

Pantic, N. K. (1956). Biostratigraphie des flores tertiaires de Serbie. *Annales Geologiques de la Peninsule Balkanique*, *24*, 199–317.

Pfahl, S., & Wernli, H. (2008). Air parcel trajectory analysis of stable isotopes in water vapor in the eastern Mediterranean. *Journal of Geophysical Research*, *113*(20), 1–16. https://doi.org/10.1029/2008JD009839

Rivas-Carballo, M. R. (1991). The development of vegetation and climate during the Miocene in the south-eastern sector of the Duero Basin (Spain). *Review of palaeobotany and palynology*, *67*(3-4), 341–351.

Rozanski, K., Araguás-Araguás, L., & Gonfiantini, R. (1993). Isotopic patterns in modern global precipitation. *Climate Change in Continental Isotopic Records*, *1–36*.

Singh, N. K., Emanuel, R. E., & McGlynn, B. L. (2016). Variability in isotopic composition of base flow in two headwater streams of the southern Appalachians. *Water Resources Research*, *52*(6), 4264–4279. https://doi.org/10.1002/2015wr018463

Stevanovic, M.P., & Pantic, N. (1954). O sarmatskoj flori i fauni iz zeleznickih useka kod Bozdarevca. *Annales Geologiques de la Peninsule Balkanique*, *22*, 53–68.

Syabryaj, S., Utescher, T., Molchanoff, S., & Bruch, A. A. (2007). Vegetation and palaeoclimate in the Miocene of Ukraine. *Palaeogeography, Palaeoclimatology, Palaeoecology*, *253*(1-2), 153–168.

Uhl, D., Bruch, A. A., Traiser, C., & Klotz, S. (2006). Palaeoclimate estimates for the Middle Miocene Schrotzburg flora (S Germany): a multi-method approach. *International Journal of Earth Sciences*, *95*(6), 1071–1085.

Utescher, T., Djordjevic-Milutinovic, D., Bruch, A., & Mosbrugger, V. (2007). Palaeoclimate and vegetation change in Serbia during the last 30 Ma. *Palaeogeography, Palaeoclimatology, Palaeoecology*, *253*(1-2), 141–152.

Utescher, T., Mosbrugger, V., & Ashraf, A. R. (2000). Terrestrial climate evolution in northwest Germany over the last 25 million years. *Palaios*, *15*, 430–449.

Valle-Hernández, M., Alonso-Gavilán, G., & Rivas-Carballo, M. R. (1995). Analyse préliminaire du Miocène dans le NE de la Dépression du Duero (aire de Belorado, Burgos, España), *Geobios*, *28*, 407–412.

Vimeux, F., Gallaire, R., Bony, S., Hoffmann, G., & Chiang, J. C. H. (2005). What are the climate controls on δD in precipitation in the Zongo Valley (Bolivia)? Implications for the Illimani ice core interpretation. *Earth and Planetary Science Letters*, *240*(2), 205–220. https://doi.org/10.1016/j.epsl.2005.09.031